Response to Reviewer #1

We thank the Reviewer #1 for his/her positive and thorough assessment of the manuscript and for the thoughtful and constructive comments.
Indeed, in the beginning we considered writing a 2-part article, but several reasons made us finally decide to submit the results in a single article. First of all, ACP does not publish technical articles, so we would have needed to submit the two parts to different journals, which would have made the review process even more complicated, and secondly, the ANN method itself is a well-established method. The novelty consists in its application by training the ANNs over a large statistics of collocated data, though limited in space and time, to develop optimized non-linear regression models to provide a more complete picture in space and time. The provided comments helped us to make the whole manuscript easier to follow. Where appropriate, we modified the text of the manuscript and the supplement with the changes marked in yellow, at the end of the response, after the point-by-point answers to each of the comments of both reviewers.

Major comments

*1. Looking at **Fig 2 and Fig S4**, there do seem to be some further physical explanations.*
*For the LW it makes sense that error would be contained to cloud top in Cbs and Ci or just below cloud base in Ci. Below these regions the LW signal will likely be mostly impacted by the high RH in the tropical atmosphere. The SW signal does demonstrate variability below Ci cloud base 400 hPa. This could be errors in representation of Ci optical depth or clouds below the Ci reflecting SW back towards TOA. Multi-layer structures are essential to represent in Ci and thin-Ci in the tropics as the majority of cirrus contain a cloud below them (as in cited Hang et al 2019). Is there a way to capture if the ANN is representing the multi-layer structures below Ci? This is mentioned briefly **around Line 445**, but did not know if this was quantifiable.*

Thank you for these extra explanations. We have improved the text accordingly in section 3.1. First of all, we have moved Fig. S3 to the main manuscript as Fig. 2. This makes it also easier to follow the discussion (see also response to major comment 7). Though we do not have any information on the cloud vertical extent, we could demonstrate that the cloud emissivity is closely related to the cloud vertical extent. It has also been shown that cloud vertical extent and number of vertical cloud layers are related (e.g. Wang et al. 2000). The neural networks seem to catch these dependencies quite well. Nevertheless, uncertainties due to these two variables which are not directly given in the input data are reflected afterwards in the predicted HRs.
Recently, we have developed ANN models to predict vertical extent and even a probability of a cloud-layer underneath, again using the same collocated AIRS-CALIPSO-CloudSat data (article in preparation). This allows a separate evaluation. For cloud vertical extent, the bias is 0 km and the standard derivations between predicted and observed vertical extent can be interpreted as uncertainties for Ci (thin Ci) of 38% (32%) over ocean and 43% (37%) over land. The hitrate for the probability of multiple cloud-layers is for Ci (thin Ci) 68% (66%) over ocean and 67% (68%) over land.

Another reason for the uncertainties is the variability of the vertical profiles of ice water content and ice crystal size distributions, which have been used to determine the FLXHR HRs, but again the input variables, like cloud emissivity and spectral cloud emissivity difference between 9 and 12 micron, only give indirect information on these.

Wang, J., W.B. Rossow, and Y. Zhang, 2000: Cloud Vertical Structure and its Variations from a 20-Yr Global Rawinsonde Dataset. J. Climate, 13, 3041-3056.

2. Section 3.3. As mentioned in the text, during ***La Nina changes the location of cloud structures****, but* ***ENSO also significantly changes the size and occurrence of MCSs over the tropical oceans due to changes in the environment*** *(e.g. Schumacher et al 2004; Henderson et al 2018; Stephens et al. 2018; Wodzkicki and Rapp 2020).* ***During La Nina the MCSs are usually more isolated and less intense****. This will likely have an impact on the observed cirrus cloud fractions. Is there a reason only one end of the ENSO spectrum was considered here? Does this case study limit the sampling of the structures?*

Schumacher, C., R. A. Houze, and I. Kraucunas, 2004: The Tropical Dynamical Response to Latent Heating Estimates Derived from the TRMM Precipitation Radar. J. Atmos. Sci., 61, 1341–1358

Henderson, D. S., C. D. Kummerow and W. Berg, 2018: ENSO influence on TRMM tropical oceanic precipitation characteristics and rain rates. J. Climate, 31, 3979–3998

Stephens, G. L., and Coauthors, 2018: Regional intensification of the tropical hydrological cycle during ENSO. Geophys. Res. Lett., 45, 4361–4370

Wodzicki, K. R., and A. D. Rapp, 2020: Variations in Precipitating Convective Feature Populations with ITCZ Width in the Pacific Ocean. J. Climate, 33, 4391–4401

Section 3.3 still belongs to the technical part. We wanted to show how for one month of data the predictions over the full CIRS swath compare to the FLXHR data over the nadir tracks. The geographical maps in Fig. 4 were only meant as an illustration, but indeed by emphasizing in the beginning that the chosen month corresponds to a La Nina situation one could have expected a comparison between El Nino and La Nina. We have changed this in the text. As you point out, there have been already so many publications about ENSO, that a new study should be more profound and is therefore beyond the scope of this publication (we added a phrase in section 4.3 with references).

3. To aid the user, how much data needs to be averaged to obtain a representative heating profile? ANNs can give a statistically representative answer, but it might take some averaging to remove the random noise. How much data, spatial and temporal, need to be averaged to remove random error and get an accurate result?

Indeed, the development of ANN regression models leads to reliable mean values. As we are interested to relate radiative heating rates of different cloud types, we have developed models separately per cloud type and separately per land and ocean to minimize biases between different scenes. As we see in the new Fig. 2 (old S3), the differences between predicted and observed radiative heating rate profiles are for all cloud types close to 0 K/day, whereas the 30% and 70% quantiles of the distributions indicate the uncertainty of individual predictions. The results in Figure 3, which presents monthly mean HR profiles for the different scenes averaged over the tropics, compare very well with the averages from the nadir tracks. So this leads to the conclusion that monthly means over the tropics (or deep tropics) are well represented, even if one distinguishes cloud types or environmental conditions. Section 4 presents results averaged over 10 to 15 years or are shown as monthly means over the time series.

4. Sec 4.2: Using warm regions and cool regions is a good way to initially separate these, but I would be careful with relating differences based on surface temperature. Other main factors, such as local environment and dynamical influences will also need to be considered. For example, MCSs in the West vs East Pacific are quite different in both surface temperature and structure due to thermal forcing in the West Pac and more dynamical forcing in the East Pac due to strong SST gradients. Further, as mentioned above (and in Section 4.3), ENSO can play a large role in the shape of MCSs due to changes in environment and regional dynamics (e.g. Schumacher et al 2004;
Henderson et al 2018; Wodzkicki and Rapp 2020). Are the two surface temp (300K vs 302K) categories here consistent in the way MCSs would be initiated? Would isolating the same comparison to a similar region yield similar differences in characteristics?

We agree completely that surface temperature is only one variable important for the onset of convection. However, recently the average of the 30% warmest SSTs have been successfully used as a proxy for tropical convective activity by Fueglistaler (2019). Over ocean our thresholds of 300K and 302K correspond to the 30% coolest and warmest ocean regions, respectively, and indeed when comparing the SSTs underneath the opaque parts (emissivity > 0.9) of the MCSs and of the coldest MCSs in the new Fig. 7, we see that these SSTs are shifted 30% towards the warmest SSTs. We have added this figure and explanations in section 4.2.

Since for land with a larger diurnal cycle and more heterogeneity, the surface temperature alone does not give information on the convective activity, we have taken out the analysis over land.

By distinguishing cooler and warmer regions we wanted to show that the results based on the predicted HRs are as expected, which gives further confidence in this new dataset.

We have also explored specific regions, as suggested. The results are displayed in Figure S11 in the supplement, with a short discussion in section 4.2. The differences in the 24-hr net radiative heating effect profiles are larger between cool and warm regions within these regions than between the average regional profiles. From this one may conclude that the on average slightly increasing HR effects of the MCS from tropical Atlantic to West Pacific can mostly be explained by increasing parts of warm SSTs from the tropical Atlantic towards the West Pacific. Differences in dynamics and atmospheric environment certainly also play a role, but this is more on the process level.

Fueglistaler, S.: Observational Evidence for Two Modes of Coupling Between Sea Surface Temperatures, Tropospheric Temperature Profile, and Shortwave Cloud Radiative Effect in the Tropics, Geophys. Res. Lett., 46, 9890-9898, https://doi.org/10.1029/2019GL083990, 2019.

5. Section 4.3 I do not think this data record is long enough to make a significant regression analysis. It is OK that these results are here, but a stronger statement on how these results seem to be linked to changes in the ONI+PDO needs to be made and that it could change with a longer record. Do the *regressions change if you break up the time periods (e.g. 2003-2012; 2007-2015; 2011-2018)? If significant regressions cannot be found the observed change with surface temperature is more likely due to natural variability. Adler et al (2017) stated that natural variability is too large to make statements on temperature and data periods longer than 30 years are needed.*

Adler, R. F., G.Gu, M.Sapiano, J.-J.Wang, and G. J.Huffman, 2017: Global precipitation: Means, variations and trends during the satellite era (1979–2014). Surv. Geophys., 38, 679–699

We agree that the record is still too short to give conclusions on climate change. We have given changes with tropical surface warming, assuming linear relationships, for comparison to other publications which are based on data records of similar length (or even shorter). We have revised section 4.3 by using now the tropical surface temperature (which is strongly correlated with global surface temperature) and have also computed the Pearson correlation coefficients for a further indication of uncertainty. We have also compared the changes with tropical surface warming between 2003-2018 with those between 2003-2014 and 2007-2018. The tendencies are the same. Furthermore we have added a correlation analysis for radiative heating averaged in the upper, middle and lower atmosphere.

6. The MCSs are defined using the presences of UT clouds and a convective core. How do you deal with cases where an MCS extends through multiple boxes? How do you ensure that cirrus is not associated with a nearby MCS and in proximity to isolated convection?

The cloud system approach consists in merging adjacent grid boxes with high-level clouds (at least 65% grid coverage) of similar height (Δp_{cld} < 50 hPa) and is explained in an earlier article (Protopapadaki et al., 2017). We have collocated the cloud system data with the ones of the HRs, so that we can associate the HRs to all grid boxes of the UT cloud systems. For the analysis of MCS we ask for at least one convective core. Indeed, multi-core convective systems may be single core systems which are connected via thin cirrus, and indeed they may be separate systems in different phases of maturity. We provide comparisons between single core results and multi-core results in Fig. 10, and see that these differences are not large.

7. The usage of supplement material needs to be streamlined somehow. There is a lot of material overall and at some points this feels like two papers that have been pushed together: one outlining the retrieval and performance and another applying the data. There is a lot of back and forth between the manuscript and supplementary material and supplemental figures seem too incorporated into the material. An example of this is the comparison of Fig. 5 and Fig. S7 or the additional information in S12 and S13. The authors compare the shapes of the heating profiles and it requires bouncing back and forth between the Supplemental and normal figures. It is described in text, but it is more useful to see the visual comparisons. Some of the Supplemental figures need to be added to main text if referenced (e.g. S12 or S13). Perhaps discussion on the performance could be added to the supplemental pages and then have the readers sent to supplemental to learn more.

Thank you for your last remark! We have revised the main manuscript, by including the figures which are necessary for the main discussions in the text, and we have added the discussions corresponding to the supplementary figures in the supplement. We have also moved the discussion on the sensitivity studies

to the selection of scenes used for the training as a separate chapter in the supplement. In this way, the technical part (section 3) should be much easier to read.
In section 4, we have revised the figures to be more concise (averaged histograms over AM and PM), and showing T_{surf}-dependent results only over ocean (see point 4). This then allows us to add maps of HRs over 3 different atmospheric layers (< 200 hPa, 200 – 600 hPa, 600 – 900 hPa).

Minor comments

Line 237: When describing the case sensitivities, it is hard to follow. A table might be easier to visualize.
We moved the description of the sensitivity study over the scenes to the supplement and have emphasized the 4 cases by building a list within the text.

Line 255: For future analysis, converting to something like sigma vertical coordinates may help mitigate this issue.
This is a very interesting suggestion; thank you! One needs an investigation if the changing pressure coordinates allow a reliable training of the ANN over all land.

Table 2 with MAE: It is hard to understand the magnitude of the error here. What is mean heating compared to the error? Fig S4, gives a slight example, but examples in the text would be useful.
The problem with the MAE is that it is a one-dimensional variable. It is used in machine learning as a metrics to get the best fit. It is the mean of the absolute errors over the 22 p-layers. For the studies in Section 4 it is more important to know the uncertainties for each of the pressure levels and for each scene type. This is shown in Fig. 2, and the HR profiles constructed over the whole tropical band in comparison with the FLXHR nadir track statistics are shown in Fig. 3.

Line 375: "The small cooling around 550 hPa is due to melting" – evidence for this?
We found one reference about this (Johansson et al. 2015) which we cite in section 4; and in section 3 we changed to 'The small cooling around 550 hPa is due to melting, owing to the transition from liquid to ice phase which occurs at or just below the freezing level at about 5 km altitude throughout the tropics, and the different emissivities of liquid and ice cause a flux divergence at that level (Tristan L'Ecuyer, personal communication).'
I discussed this with Tristan L'Ecuyer in 2017, who wrote: 'This is in fact a radiative effect owing to the transition from ice to liquid phase in mostly the surrounding stratiform areas of convective systems. In that case most melting occurs at or just below the freezing level and the different emissivities of liquid and ice cause a flux divergence at that level, which happens to occur at 5 km throughout the year in the tropics.'

Section 4.2 I would remind the readers here that this data is much longer than other vertically resolved datasets.
Actually this is most important for section 4.3, when we show the time series, but you are right; our statistics is much higher than what was published before.

Figures: Differentiating solid vs broken lines is difficult in the legends.
Figures redone

Line 544: Is T < 210 K cloud top temperature?
The IR sounder retrieval does not provide the cloud top temperature, but corresponds to a height where the cloud reaches an optical depth of about 0.5, which corresponds to about 1.5 – 2 km below cloud top (Stubenrauch et al. 2017). We have changed this in the text to ‘cold MCSs with near-cloud top temperature < 210 K’.

Response to Reviewer #2

We thank the Reviewer #2 for the thoughtful and constructive comments concerning our manuscript. Indeed, the ANN method itself is a well-established method. The novelty consists in its application by training the ANNs over a large statistics of collocated data, though limited in space and time, to develop optimized non-linear regression models to provide a more complete picture in space and time. The provided comments helped us to improve the manuscript for clarity. Where appropriate, we modified the text of the manuscript and the supplement with the changes marked in yellow. This marked text together with the new figures are provided at the end of the response to reviewer #1. Below, we provide point-by-point answers to each of the comments of reviewer #2.

Major comments

1. Section 2.1: This section should be shortened and only the key facts of the CRIS data set relevant for the interpretation of the results should be mentioned. The other part can be moved to the supplement part. Line 90: Is the information about AMSU relevant for CIRS, if yes, this yields to some restrictions for the application of the new ANN-based method.

First, we have added a short paragraph just after the title of section 2, which gives the purpose of the subsections. Section 2.1 describes the CIRS cloud data which are used as input for the machine learning as well as the cloud system data derived from the CIRS data which are used in the analysis of section 4. As both datasets are already published, we have shortened the whole section.

No, we don't use AMSU data. The sentence was there only to explain the grouping of 3 x 3 AIRS measurements. As this information is not relevant for the rest of the article, we have taken out this sentence.

2. Section 2.2: This section can also be shortened or some parts can be moved to the supplement. E.g. the ERA-Interim description, TIGR data set.

We have considerably shortened this section, as the ERA-Interim data are published elsewhere. We describe shortly all variables which are used as input parameters in the ANN models. However, we did not move the removed parts to the supplement, as the supplement is already quite long.

3. Section 2.3: This section can also be shortened or some parts can be moved to the supplement.

This section describes the target data as well as their quality. We also shortened this section, but we kept the description of how the radiative heating rates were determined as well as a summary of their evaluation.

All in all, we restructured and shortened sections 2.1-2.3 by more than 20% and hope that the new description is easier to read.

4. Line 223 ff: the absolute number of pattern (samples for training/test/validation) should be given. These values are important for the interpretation of the results in Tab. 2 as well as for Fig. S1 and S2. For the *latter ones, it should be explained why the number of epochs is different for the different data sets and what was the stopping criteria for the training of the ANN.*

The four years of collocated data correspond to a very large statistics of more than 16 million data points. We added this information in the first paragraph of section 2.4. When separating by scene type, the samples vary from 94000 Cb samples over land to 4.8 million mid- and lowlevel cloud samples over ocean. These samples contain both, AM and PM data. For the training of the SW heating rates, only half of the data are used (PM), which still leaves very large samples.

The number of epochs to converge towards a minimum loss is relatively small: less than 60 for cloudy scenes (Figure S1) and less than 45 for clear sky scenes (Figure S2). Essentially, the MAE decreases considerably only within the first 10 (5) epochs for cloudy (clear sky) scenes. The relatively small number of epochs necessary for convergence may be explained by the large statistics we use for the training and the number of relevant variables for the prediction.

5. Line 280 ff.: The different types of models should be given in a bullet list or table with corresponding labels given in Tab. 2 and streamlined with the labels in Fig. S1, S2.

We have summarized the sensitivity experiments with the corresponding variables also in Table 1. In the supplement we added a text for the description and interpretation for Figures S1 and S2, as well as an assignment of the labels to the experiments.

6. Tab. 2 & 3: In these tables as well as in the discussion of it, relative error measures should be given, too. It would be good in order to judge the approximation and generalisation accuracy of the ANN it would be good to have the mean absolute percentage error (MAPE) in addition.

As we discuss in section 3, the average MAE over the vertical HR profiles is only one criterion to choose the best model for the prediction of the vertical HR profiles. In the beginning we also considered percentage errors, but the problem is that all cloud types and clear sky have at some vertical layer a value near 0. In particular for Cb, the lower layers have HRs close to 0. This would make an interpretation of the MAPE quite difficult. MAPE values would be automatically larger for profile types with more small HR values within the troposphere. In order to get reasonable MAPE values one has to introduce a lower absolute limit of the HR values. Considering the new Figures S3 and S4, which present the difference between predicted and observed HR profiles as well as the HR profiles, for Cb for example the difference is close to 0 for layers below an altitude of 800 hPa, while their HRs are also close to 0, leading to an artificially large percentage error. For Cb the maximum LW HR bias of the Cb model (red) is about 0.25 K/day for an average LW HR of -3.5 K/day and the maximum SW HR bias is about 0.5 K/day for an average SW HR of about 4 K/day. This corresponds to a percentage error of 7% and of 13%, respectively. As we use the same metrics in the tables, we can compare the performances of the models using different sets of variables. Figures S3 and S4 make it possible to roughly compute the percentage errors for different layers. MAPE may be a very useful metrics for other applications, but we do not see what the additional computation of MAPE would add to the interpretation of our results.

7. Fig 13 & 14: It is hard to compare the different panels of these figures and the usage e.g. for upcoming climate studies. It would be better to have only one panel of the total net HR. Furthermore in order to judge the influence of the ENSO index, PDO and surface temperature (see Fig. 12) to total net HR over time in a more quantitative way, mean total net HR time series data for different pressure layers (e.g. low, middle, high) should be correlated to the time series data of Fig. 12.
We now only show the 24-hr net radiative heating effects. In addition, we have added time series of the net HRs integrated over three vertical layers (100 - 200 hPa, 200 – 600 hPa, 600 – 900 hPa) and have computed correlation coefficients with the different other variables.

Minor comments
Line 237: Line 255 ff. There are techniques available to deal with partly missing values in the target vector. The target vector can be masked for valid/not valid training value in the target vector. Then only for the valid elements in the target vector, the error in backpropagated during training. For not valid elements (NaN) the error is set to zero. This is a proven concept for training of ANN with incomplete target vectors.
Thank you for this information. The authors were not aware of this, even after having discussed with several AI experts. Therefore we have used another method (replacing invalid values below the surface by mean values classified per month and scene type), which is perhaps less elegant but should give similar results.

Line 423 & 424: ".. is 24% larger, larger than 21% found by Li … " needs some clarification
We have redone the computations by using a LW average over AM and PM (instead of only PM) and added uncertainty estimates from clear sky identification and diurnal cloud amount variability. The final result lies between 20 and 25%, or 22 ± 3 %, which is only slightly larger than 21%. However the shape of the HR profile is different compared to the result of Li et al..

Line 578: data processed for 30N to 30S; but only results of latitude band 15N to 15S are shown (Fig. 10).
We have added maps which show results between 30N and 30S. We have mostly shown results for the deep tropics, as these have been shown by Li et al. 2013.

Fig. 7: the data sources should be mentioned in more detail.
Precipitable water and surface temperature are from ERA-Interim and UT cloud frequency of occurrence from CIRS.

The quality of some figures should be improved e.g. Fig. 6 (use of vector instead of raster graphics is highly recommended)
redone.

Recommendation:

The developed method to derive high resolution 3D HR in the inner tropics uses a lot of different model data: CRIS, ERA-interim, MOIDS AOD. Each of the models mentioned has its own errors and bias which are described well in paper. ANN can handle systematic model error of the input data well, but if one or more models will change over time (which is likely for such kind of long term data sets) the trained ANN model for the generation of 3D HR data will generate most likely biases. ANN are also not able to cope for random errors in the model input data.

This can be omitted if the original satellite data (in this case AIRS spectral radiance data) are used with full spectral resolution as input data. This makes the ANN HR model more applicable and more robust especially in order to transfer this approach to other IR sounder data (e.g. IASI) for further studies. For transfer of a trained ANN model on AIRS data e.g. transfer learning techniques can be used to adapt it for IASI.

We decided to use physical variables instead of radiances for different reasons. We use CIRS cloud data, retrieved from AIRS or IASI, together with ERA-Interim atmospheric and surface data. The latter have been also used as ancillary data in the CIRS retrieval, which gives a certain coherence. We tested two additional variables, vertical velocity from ERA5 and monthly mean AOD from MODIS, but finally we do not use them in the final models, as we could not detect a considerable improvement. We have been careful to only select variables which are also available for the CIRS-IASI data, so that the same models can be applied on IASI data. For the evaluation we need then independent data, as IASI and CALIPSO-CloudSat data do not overlap in the tropical band. We foresee to use ARM data for an independent evaluation, though these also have their issues, as mentioned in sections 2.3 and 4.1.

We agree that we could have used the radiances as input parameters, but it would have been technically much more complicated for us, as we would have needed to download the full AIRS and IASI spectra (2378 channels and 8461 channels, respectively) and then choose the most relevant channels for the training of the ANN models. As we have trained models for different cloud types and clear sky, for the reasons described in our manuscript (for example Cb is very rare, with less than 10%), we would have needed anyway the CIRS data for the distinction of scene types. Furthermore it would have needed additional care to adapt the IASI spectral channels to those of AIRS in order to use the same models. As our funding is very limited (the three co-authors worked each only 6 months on this project), we decided to use the information which was easily available and which is also used in combination for further studies.

3D Radiative Heating of Tropical Upper Tropospheric Cloud Systems derived from Synergistic A-Train Observations and Machine Learning

Claudia J. Stubenrauch[1], Giacomo Caria[1], Sofia E. Protopapadaki[2], Friederike Hemmer[1]

[1]Laboratoire de Météorologie Dynamique / Institut Pierre-Simon Laplace, (LMD/IPSL), Sorbonne Université, Ecole Polytechnique, CNRS, Paris, France
[2]COOPETIC, Paris, France

Correspondence to: Claudia J. Stubenrauch (stubenrauch@lmd.polytechnique.fr)

Abstract. Upper Tropospheric (UT) cloud systems constructed from Atmospheric Infrared Sounder (AIRS) cloud data provide a horizontal emissivity structure, allowing to link convective core to anvil properties. By using machine learning techniques we composed a horizontally complete picture of the radiative heating rates deduced from CALIPSO lidar and CloudSat radar measurements, which are only available along narrow nadir tracks. To train the artificial neural networks, we combined the simultaneous AIRS, CALIPSO and CloudSat data with ERA-Interim meteorological reanalysis data in the tropics over a period of four years in order to train artificial networks. The resulting non-linear regression models estimate the radiative heating rates as a function of about 40 cloud, atmospheric and surface properties, with a column-integrated mean absolute error (MAE) of 0.8 K/d (0.5 K/day) for cloudy scenes and 0.4 (0.3 K/day) for clear sky in the longwave (shortwave) spectral domain. Developing separate models for i) high opaque clouds, ii) cirrus, iii) mid- and low-level clouds and iv) clear sky, independently over ocean and over land, leads to a small improvement, when considering the profiles. These models were applied to the whole AIRS cloud dataset, combined with ERA-Interim, to build 3D radiative heating rate fields. Over the deep tropics, UT clouds have a net radiative heating effect of about 0.3 K/day throughout the troposphere from 250 hPa downward. This radiative heating enhances the column-integrated latent heating by about 22% ± 3%. While in warmer regions the net radiative heating profile is nearly completely driven by deep convective cloud systems, it is also influenced by low-level clouds in the cooler regions. The heating rates of the convective systems in both regions also differ: In the warm regions the net radiative heating by the thicker cirrus anvils is vertically more extended and their surrounding thin cirrus heat the entire troposphere by about 0.5 K/day. The 15-year time series reveal a slight increase of the vertical heating in the upper and middle troposphere by convective systems with tropical surface temperature warming, which can be linked to deeper systems. In addition, the layer near the tropopause is slightly more heated by increased thin cirrus during periods of surface warming. While the relative coverage of convective systems is relatively stable with surface warming, their depth increases, measured by a decrease of their near top temperature of -3.4 ± 0.2 K/K. Finally, the data reveal a connection of the MCS heating in the upper and middle troposphere and the (low-level) cloud cooling in the lower atmosphere in the cool regions, with a correlation coefficient equal

to 0.72, which consolidates the hypothesis of an energetic connection between the convective regions and the subsidence regions.

1 Introduction

Upper tropospheric (UT) clouds play a vital role in the climate system by modulating the Earth's energy budget and the UT heat transport. These clouds cover about 30% of the Earth and even 40% of the tropics (e. g. Stubenrauch et al. 2013, 2017). Yet, their role in the climate change feedback is still highly uncertain (e. g. Boucher et al., 2013, Zelinka et al., 2016). Tropical organized deep convection leads to cloud systems with stratiform cirrus anvils of the size of several 1000's km^2 (e.g. Houze, 2004). Living much longer than the convective towers themselves, these cirrus anvils produce a radiative heating that is expected to be as important for the large-scale circulation as the released latent heat in the initial stage of convection. In tropical convective regions more than 50% of the total heating is contributed by cirrus radiative heating (e.g. Sohn 1999). This heating, induced by the anvils and cirrus, then influences the large-scale tropical atmospheric circulation (e.g. Slingo and Slingo, 1991; Sherwood et al., 1994). It is affected by: i) the areal coverage, ii) the horizontal cloud emissivity structure within the systems, and iii) the vertical structure of the cirrus anvils (layering and microphysics). The influence of the vertical distribution of radiative heating was demonstrated on large-scale tropical circulations by Stephens and Webster (1984) and Bergman and Hendon (2000) and on the local cloud structure by Mather et al. (2007). The net radiative heating associated with tropical anvils and cirrus layers is also known to play a major role in the thermodynamic stability of the upper troposphere (Ackerman et al., 1988) and self-regulation of tropical convection (e.g. Stephens et al., 2004, 2008).

So far, observational studies of tropical mesoscale convective systems (MCSs) have concentrated on the convective towers and the thick cirrus anvils (e.g. Yuan and Houze 2010, Roca et al. 2014). Yet thin cirrus correspond to about 30% of / around the anvil area of the deep convective systems (Protopapadaki et al. 2017). Other studies, focusing on their vertical structure along narrow nadir tracks (Fig. 1), missed the lateral horizontal dimension (e.g. Igel et al., 2014; Stein et al. 2017). The organisation of convection was studied by statistical analysis of 'cloud regimes', defined by similar cloud property distributions within grid cells (e.g. Tselioudis et al. 2013, Tan et al. 2015, Oreopoulos et al., 2016). Suggesting a connection between radiative effects and dynamics, this concept is very valuable, but it misses the horizontal extent of the systems.

A study by Li et al. (2013) finds that the column-integrated radiative heating of tropical UT clouds accounts for about 20% of the latent heating. The radiative heating was estimated by combining International Satellite Cloud Climatology Project (ISCCP) data, classified as four distinct cloud regimes at a spatial resolution of 2.5° latitude and longitude, with heating rate profiles assigned from two tropical Atmospheric Radiation Measurement (ARM) sites, while the latent heating was deduced from measurements of the Tropical Rainfall Measuring Mission (TRMM) Precipitation Radar (PR). However, ISCCP and ARM data both may underestimate the effect of thin cirrus, because its occurrence may be missed by ground observation

(Protat et al., 2014) and by ISCCP (e.g. Stubenrauch et al., 2013), in particular when low-level clouds are also present and during night.

Therefore, to include also the thinner cirrus and the complete 3D structure of these cloud systems, we applied a different strategy: To estimate the radiative heating rates of UT clouds we combined observations which are more sensitive to thin cirrus, together with machine learning techniques and a cloud system approach. The good spectral resolution of IR sounders makes them sensitive to cirrus, down to a visible optical depth of 0.2, during daytime and nighttime. Cloud properties retrieved from measurements of the cross-track scanning Atmospheric Infrared Sounder (AIRS) aboard the polar orbiting Aqua satellite have a large instantaneous horizontal coverage (Stubenrauch et al., 2017). They have been used by Protopapadaki et al. (2017) to reconstruct UT cloud systems. Recently these datasets have been extended, so that they now cover Sep 2002 to Aug 2019. On the other hand, the space-borne active lidar and radar measurements of the CALIPSO and CloudSat missions (Stephens et al., 2018a) supply the cloud vertical structure, in particular the radiative heating rates (Henderson et al., 2013). As this information is only available along successive narrow nadir tracks, separated by about 2500 km, we employed machine learning techniques on cloud, atmospheric and surface properties to build a 3D description of these cloud systems. These techniques were already successfully applied to extend IR brightness temperature (Kleynhans et al., 2017) and snow water (Snauffer et al., 2018) from other atmospheric variables.

This article presents the effect of UT clouds on tropical radiative heating rates in the longwave (LW) and shortwave (SW) spectral domain and the relationship between surface temperature, convective depth and anvil radiative heating / cooling. Section 2 describes the data which are used as input and target for the training of the neural networks, which themselves are also explained. Sensitivity studies and evaluation of these developed non-linear regression models are presented in Section 3. They give insight into the most appropriate cloud and atmospheric properties as well as on how many scene-dependent non-linear regression models are necessary to reliably predict the radiative heating rates of different cloud types. After application of these models to the 15-year time period of AIRS cloud data, combined with ERA-Interim atmospheric and surface data, section 4 highlights results on the contribution of clouds, and in particular of MCSs, on the tropical radiative heating / cooling. Conclusions and an outlook are given in Section 5.

2 Data and Methods

The different variables to be used for the prediction of the radiative heating rates are described in sections 2.1 and 2.2. Section 2.1 also presents cloud system data used in the analysis in section 4. The target data are presented together with their uncertainties in section 2.3. Finally the neural network construction is given in section 2.4.

SECTIONS 2.1-2.3 HAVE BEEN SHORTENED BY 20%

2.1 AIRS Cloud Data and Cloud System Data

Since 2002 AIRS (Chahine et al., 2006) aboard the National Aeronautics and Space Administration (NASA) Earth Observation Satellite Aqua provides very high spectral resolution measurements of Earth emitted radiation in the thermal IR (3.74 – 15.40 μm) at 1:30AM and 1:30PM local time (LT). Cross-track scanning leads to a large instantaneous coverage of about 70% in the tropics. The spatial resolution of these measurements at nadir is about 13.5 km.

The Clouds from IR Sounders (CIRS) data (Stubenrauch et al., 2017) provide cloud pressure (p_{cld}), cloud emissivity (ε_{cld}), as well as cloud temperature (T_{cld}) and cloud height (z_{cld}), together with their uncertainties. The cloud retrieval is based on a weighted χ^2 method (Stubenrauch et al., 1999), which uses eight channels along the 15 μm CO_2 absorption band, with peak contributions between 235 hPa and near the surface. UT clouds are defined as clouds with p_{cld} < 440 hPa. They are further distinguished with respect to ε_{cld} as opaque high clouds (Cb, $\varepsilon_{cld} \geq 0.98$), cirrus (Ci, $0.98 < \varepsilon_{cld} \leq 0.5$) and thin cirrus (thCi, $0.5 < \varepsilon_{cld} \leq 0.1$). p_{cld} is transformed to T_{cld} and z_{cld} via the atmospheric temperature and water vapour profiles of ancillary data (see section 2.2). An 'a posteriori' multi-spectral cloud detection is based on the spectral coherence of retrieved cloud emissivity in the atmospheric window between 9 and 12 μm. This spectral region also provides information on the thermodynamic phase of the clouds, and for semi-transparent cirrus the slope of cloud emissivities between 9 and 12 μm gives an indication of the effective ice crystal diameter (Guignard et al. 2012). The CIRS cloud data are retrieved per AIRS footprint.

In order to obtain information on the surrounding cloud scene structure, sixteen cloud regimes are distinguished by applying a k-means clustering on histograms of ε_{cld} and p_{cld} within regions of 2° latitude x 2° longitude, similar to the method developed by Rossow et al. (2005) using ISCCP data. In addition, we provide the clear sky fraction estimated from AIRS within these grid cells.

For the analysis in section 4, we combine the resulting radiative heating rate fields with information on UT cloud systems. Their reconstruction is based on two independent variables, p_{cld} and ε_{cld} (Protopapadaki et al. 2017): The AIRS cloud data were merged to grid cells of 0.5° latitude x 0.5° longitude, and then data gaps between adjacent orbits were filled. Only grid cells containing more than 70% UT clouds were kept to reconstruct UT cloud systems from adjacent elements of similar cloud height, given by p_{cld}. Convective cores, thick cirrus and thin cirrus within the anvils are identified by ε_{cld} intervals, with thresholds at 0.98 and 0.5. This cloud system concept is used in section 4 to identify MCSs and to relate the radiative heating / cooling profiles of their convective cores and their anvils to different surface conditions. Therefore MSCs were defined as UT cloud systems with at least one convective core (built from grid cells with average ε_{cld} > 0.98 within subregions of ε_{cld} > 0.9).

2.2 Atmospheric and surface data

Atmospheric profiles as well as surface pressure and temperature are used as ancillary data for the CIRS retrieval. These values are provided by the ERA-Interim atmospheric reanalysis data of the European Centre for Medium-Range Weather Forecast (Dee *et al.* 2011), given at a spatial resolution of 0.75° latitude x 0.75° longitude and four times per day. We interpolated the atmospheric profiles of temperature and water vapour to 23 pressure levels and derived the relative humidity within the 22 atmospheric layers from the temperature and water vapour profiles by a method based on (Stubenrauch and Schumann, 2005). The CIRS cloud retrieval classifies the atmospheric profiles by comparing them to about 2300 representative clear sky atmospheric profiles of the Thermodynamic Initial Guess Retrieval (TIGR) data base (Chédin et al. 2003), to choose the corresponding spectral atmospheric transmissivities for the radiative transfer in the retrieval. This atmospheric classification provides additional information for the non-linear regression models developed in section 3.

For the prediction of LW heating rates over land we use spectral IR surface emissivities at wavelengths around 9.00, 10.16 and 12.18 μm, retrieved from IR Atmospheric Sounding Interferometer (IASI) measurements (Paul et al., 2012) and given as a monthly mean climatology at a spatial resolution of 0.25° x 0.25°. Over water, the surface emissivity is set to 0.99 at 9 μm and to 0.98 at the two other wavelengths, according to Wu and Smith (1997).

For the prediction of the SW heating rates during daytime we use the visible surface albedo at noon local solar time and the solar zenith angle. The land surface albedos, retrieved from Moderate Resolution Imaging Spectroradiometer (MODIS) measurements (MODIS Collection 5, MOD43 product, Strahler et al., 1999), are distributed as a monthly climatology at a spatial resolution of 0.1° x 0.1° by the NASA Earth Observations (NEO) website (https://neo.sci.gsfc. nasa.gov/). Over ocean we assume a surface albedo at noon local solar time of 0.06.

In order to explore the benefit of adding the aerosol optical depth (AOD) to the input variables, we use a monthly climatology of AOD from MODIS (MODIS Collection 5, MOD04/MYD04 product, Levy et al., 2009) at a spatial resolution of 0.25° x 0.25°, also distributed by the NEO website.

Finally we investigate the value of adding the vertical velocity at 500 hPa as input variable, given at the spatial resolution of 0.375° x 0.375°, from the ERA5 reanalysis (Hersbach et al., 2020).

2.3 CALIPSO-CloudSat vertical structure and collocation with AIRS

The vertical structure of the clouds can only be determined by active spaceborne instruments. The Cloud-Aerosol Lidar with Orthogonal Polarization (CALIOP) aboard CALIPSO and the Cloud Profiling Radar (CPR) aboard CloudSat, both part of the A-Train constellation, follow AIRS within a few minutes. CALIOP provides backscatter profiles at a wavelength of 532 nm and 1064 nm. The backscatter ratio helps to distinguish between aerosols and clouds. The 94 GHz nadir-viewing CPR measures profiles of the power backscattered by clouds at a native vertical resolution of 480 m over footprints covering 1.8 km×1.4 km.

By using oversampling, data are provided at a vertical resolution of 240 m. Combining information from both instruments allows a complete description of the cloud vertical structure. However, this information is only given along successive nadir tracks.

We extended the collocated AIRS-CALIPSO-CloudSat data used by Feofilov et al. (2015) and Stubenrauch et al. (2017) by the NASA 2B FLXHR-LIDAR (R04) heating rates for the period of 2007 to 2010. These vertical profiles have about 80 values over a height of 20 km. Since the AIRS cloud height is retrieved as pressure and the input parameters are not precise enough to predict such a fine vertical structure, we transformed the FLXHR-LIDAR heating rates to 22 pressure layers between 70 hPa and the surface. For each of the AIRS footprints this collocated dataset also includes the number of detected cloud layers, from the 2B-GEOPROF-LIDAR data, used in section 3 to evaluate the clear sky identification by AIRS alone.

The radiative fluxes and heating rates of 2B-FLXHR-LIDAR (version R04; Henderson et al., 2013; L'Ecuyer et al., 2008) were derived by applying the BUGSrad broadband radiative transfer model (Ritter and Geleyn, 1992) to the scenes observed by CALIPSO-CloudSat, using as inputs the vertical location of the cloud layers (2B-GEOPROF-LIDAR; Mace et al., 2010), the cloud water / ice content and effective particle sizes retrieved from radar only (2B-CWC-RO; Austin et al., 2009), distinction between cloud and rain water contents from 2C-PRECIP-COLUMN (Haynes et al, 2009) and collocated atmospheric and surface auxiliary data from ECMWF. For the clouds and aerosols which are undetected by CloudSat, the MODIS-based cloud optical depth (2B-TAU) and CALIPSO version-3 products (Trepte et al., 2010) are used to calculate the corresponding radiative properties. The phase of thin clouds only detected by CALIPSO is set to ice for $T < 253.15$ K, and their ice crystal equivalent mass sphere effective radius is assumed to be 30 μm.

The comparison of 2B-FLXHR-LIDAR (R04) with CERES-CALIPSO-CloudSat-MODIS (CCCM) products, using a finer vertical resolution and different microphysics than FLXHR-LIDAR, revealed a small low bias in SW heating of FLXHR-LIDAR due to a slight underestimation of cloud occurrence of height below 1 km, while the LW heating of CCCM for thin cirrus is slightly larger (Ham et al., 2017).

Over the tropical ARM site of Darwin, Protat et al. (2014) found a good agreement between the shapes of the 2B-FLXHR-LIDAR radiative heating rates and those derived from ground-based remote sensing (McFarlane et al., 2013) and from an experimental 2C-ICE-FLUX product for altitudes between 1 and 12 km. Above 12 km, in comparison to 2B-FLXHR-LIDAR, the underreported cirrus frequency by the ground-based lidar leads to a negative bias of 0.4 to 0.8 K/day in the LW heating rates, whereas different microphysical properties of thin cirrus in 2C-ICE-FLUX produce about 0.3 K/day larger LW heating rates. The same 2C-ICE microphysical properties (Deng et al., 2013), together with improved cloud phase identification and surface characteristics, are integrated in the very recently released version R05 of FLXHR-LIDAR data (Matus and L'Ecuyer, 2017). The improvements lead to a slightly better agreement with TOA fluxes from the Clouds and the Earth's Radiant Energy System (CERES), and the global annual mean atmospheric cloud radiative effect between both versions differs by about 10% (Hang et al., 2019): 7.8 Wm^{-2} (R05) compared to 8.6 Wm^{-2} (R04). As version R05 of the FLXHR-LIDAR data was only released when we were finishing our analyses of section 4, we present the results which used 2B-FLXHR-LIDAR (R04) data for the training of the artificial neural networks (ANN), keeping in mind that the cirrus HRs above a height corresponding to 200 hPa are more reliable than those from ground-based measurements, but may be still slightly underestimated compared to newer versions with different ice microphysics (Protat et al., 2014; Ham et al., 2017; Hang et al., 2019). Within the overall uncertainties described in this section and in section 3, the results in section 4 are still valid.

2.4 Artificial Neural Network Construction

The challenge in creating a complete 3D description of the UT cloud systems and their environment lies in the lateral expansion of the information on the vertical structure, only available at the locations sampled along the lidar-radar nadir tracks. Figure 1 illustrates the collocation of vertical heating rates deduced from lidar-radar along these tracks and horizontal cloud information from IR sounders. In order to achieve our goal of creating complete 3D heating rate fields, we developed nonlinear regression models based on ANNs which use as input the combined AIRS and ERA-Interim data described in sections 2.1 and 2.2. ANNs have seen spectacular progress during the last few years, especially in the automation of finding the most appropriate weights used in the ANN layers. We used the TensorFlow framework (https://www.tensorflow.org) to train machine learning models with the help of the Keras program library (https://keras.io) for Python, with training and testing along the nadir tracks. The four years of collocated data correspond to a very large statistics of more than 16 million data points. When developing scene type dependent models in section 3.2, samples vary from 4.8 million data points for mid- and low-level clouds over ocean to 94000 data points for Cb over land.

Kleynhans et al. (2017) demonstrated that thermal IR radiation at top of atmosphere, measured by MODIS, can be best simulated from available atmospheric reanalysis data by using a multi-layer perceptron (MLP) supervised learning technique. This technique produced the lowest overall error rates, in particular over cloudy situations, compared to non-linear support vector regression (SVR), convolutional neural network (CNN) and even to atmospheric radiative transfer simulations.

After having tested the MLP performance on the number of hidden layers within the ANN, our final ANN consists of an input layer with the approximately 30 to 45 input variables (see section 3), two hidden layers with 64 neurons and an output layer which corresponds to the radiative heating rates given in 22 pressure layers. To improve the performance, we used the rectified linear unit (ReLU) layer activation function. For a better efficiency we use the Adaptive Moment Estimation (Adam) optimizer, using adaptive learning rates (Kingma and Ba, 2014).

The training dataset is randomly separated into three portions: 80% are used for training, 10% for validation and 10% for testing. In order to have similar cloud type, day-night and ocean-land statistics in these portions, we stratified the data by cloud type, ocean-land and day-night for LW and by cloud type and ocean-land for SW (only available during daytime). The model parameters are fitted by minimizing a loss function, which corresponds to the average of the squared differences between the predicted heating rates and the target values from the lidar-radar observations of the 22 pressure layers. For the determination of the quality of the resulting regression models we use then as metrics the average of the 22 mean absolute errors (MAE) between the prediction values and the target values. In order to avoid overfitting, we stop the fitting when the minimum loss does not further improve during ten iterations (epochs).

As many input variable distributions are not Gaussian, and to avoid outliers, we standardized the input variables by subtracting an 'acceptable' minimum and then dividing by the difference between 'acceptable' variable maximum and minimum. These acceptable minimum and maximum values have been established for each variable and adapted to the scenes for which the models were trained: ocean or land, all cloud types, clear sky, high clouds or mid- and low-level clouds. Before the application of the model, all input variables are first bounded between these minimum and maximum values.

3 Sensitivity Studies and evaluation

We assessed the sensitivity of the predicted radiative heating rates (HRs) to the selection of input variables (section 3.1). In general, a model trained over all clouds over ocean and land together soothes out differences between different cloud types and between ocean and land. Furthermore scenes which are less frequent may have a smaller weight and may be therefore less represented than other scenes. Since we are interested in the study of the effect of UT cloud systems, we chose to develop separate MLP ANN models for

i) Cb
ii) Ci and thin Ci
iii) mid- and low-level clouds
iv) clear sky

each separately over ocean and over land, leading to eight models. Comparisons of these models with those developed for all clouds together are on average small and are described in the supplement, while the evaluation of the final eight models is given in section 3.2. The cloud and clear sky models were then combined to construct the radiative HRs over the whole tropical band (section 3.3).

3.1 Sensitivity to input variables

The input variables describing the cloud, atmosphere and surface properties used for the prediction of the radiative HRs are summarized in Table 1.

The training for the SW HRs is based only on data recorded at 1:30PM LT, while the training for the LW HRs exploits data for both 1:30AM and 1:30PM. Since the CALIPSO data are slightly more sensitive during night-time, we used for the LW training a day-night flag as additional input variable. The choice of input variables slightly differs for the prediction of LW and SW HRs: For the training of LW HRs, we used surface spectral IR emissivities while for the training of SW HRs we used surface albedo and solar zenith angle.

The MLP regression models compute radiative HRs for 22 pressure layers from 70 hPa to 1000 hPa, using about 40 input variables. Earth topography implies that the temperature, relative humidity and radiative HR profiles are not always determined over all 22 pressure layers. Given that neural networks need a constant number of input and output values, we had to replace the missing values below the surface. Therefore, we first continued the temperature, relative humidity and radiative HR profiles below p_{surf} with their lowest valid value, and then added to these values the average vertical gradients between the corresponding layer and the layer with the lowest valid value. These gradients were computed using the average profiles of regions containing all 22 pressure layers, separately determined over ocean and over land, and per cloud type and month. Even if these values below the surface are not used in the analyses, they slightly influence the training.

Table 1: List of input variables for the prediction of LW / SW heating rates and sensitivity experiments.

Input variables			
Clouds			
CIRS cloud properties and uncertainties		ε_{cld}, p_{cld}, T_{cld}, $d\varepsilon_{cld}$, dp_{cld}, dT_{cld}, χ_{min}^2	
cloud spectral emissivity difference		$(\varepsilon_{cld}$ (12µm) - $(\varepsilon_{cld}$ (9µm))	
CIRS cloud regime (CR) at 2° x 2°		CR (1-16), kernel distance	
Atmosphere			
AIRS T_B at 0.5° x 0.5°		T_B(11.85µm), $\sigma(T_B)$, T_B(7.18 µm)	
ERA-Interim atmospheric properties		TIGR atmosphere (1-1500), total precipitable water, $p_{tropopause}$	
ERA-Interim relative humidity profile		RH (determined from T and water vapour) within 10 layers	
ERA-Interim temperature profile		T within 10 layers	
ERA5 vertical velocity		ω at 500hPa	
MODIS aerosol optical depth		AOD (monthly mean climatology)	
Surface			
ERA-Interim surface properties		p_{surf}, T_{surf}, nb of atm. layers down to p_{surf}	
IASI spectral surface emissivity		ε_{surf}(9, 10, 12µm)	(monthly mean climatology)
surface albedo		α_{surf}	(monthly mean climatology)
solar zenith angle, day-night flag, land-ocean flag			
Sensitivity experiments			
1) basic variables	(18/19)	ε_{cld}, p_{cld}, T_{cld}, $d\varepsilon_{cld}$, dp_{cld}, dT_{cld}, χ_{min}^2, $(\varepsilon_{cld}$ (12µm) - $(\varepsilon_{cld}$ (9µm)), T_B(11.85µm), $\sigma(T_B)$, T_B(7.18 µm), TIGR atmosphere, total precipitable water, $p_{tropopause}$, p_{surf}, T_{surf}, nb of atm. layers down to p_{surf}, day-night (+solar zenith angle)	
2) +CR	(20/21)	basic + cloud regime + kernel distance	
3) +RH10	(30/31)	basic + CR + RH profiles in 10 layers	
4) +T10	(40/41)	basic + CR + RH10 + T profiles in 10 layers	
5) +w500	(41/42)	basic + CR + RH10 + T10 + ω at 500hPa from ERA5	
6) +AOD	(42/43)	basic + CR + RH10 + T10 + w500 + monthly mean AOD	

For the sensitivity study of the most appropriate variables (Table1), we considered cloudy scenes over ocean, and we set up six different experiments to predict the LW (SW) HRs, starting with

1) a set of 18 (19) basic variables, which describe cloud, atmospheric and surface properties: CIRS cloud properties and their uncertainties, cloud spectral emissivity difference between 9 and 12 μm, AIRS brightness temperatures, total precipitable water, tropopause height and TIGR atmosphere class, surface pressure and temperature.

Then we gradually added to the basic variables of experiment 1:

2) cloud regime classification and its uncertainty given by the kernel distance: total of 20 (21) input variables,

3) relative humidity in ten layers: total of 30 (31) input variables,

4) atmospheric temperature in ten layers: total of 40 (41) input variables,

5) vertical velocity from ERA5 reanalyses: total of 41 (42) input variables, and

6) monthly mean aerosol optical depth: total of 42 (43) input variables.

Table 2 compares the mean absolute error (MAE) for the prediction of LW and SW heating rates of clouds over ocean from the experiments 1 to 6. In all cases the MAE over the validation data and over the testing data are within 0.01 K/d. The MAE over the testing dataset is shown. The similarity in MAE between the validation and testing data means that there is no under-fitting (the variables are not sufficient to predict the target) nor over-fitting (the model is too detailed, with too many variables or the data base is not sufficiently large). As shown in Table 2, the MAE decreases by about 5% (10%) for the LW (SW) model when the atmospheric profiles are included. The addition of vertical velocity and AOD do not seem to improve the results. This lack of improvement may be explained by noise coming from these sources in combination with the AIRS cloud properties and ERA-Interim atmospheric and surface properties. The addition of the temperature profile only slightly improves the prediction of the heating rates, most probably because the atmospheric T profiles are more similar within the tropics than the atmospheric relative humidity profiles.

Table 2: MAE (K/day) for the prediction of LW or SW heating rates of clouds over ocean, from experiments 1 - 6.

ocean	**basic**	**+ CR**	**+ RH10**	**RH-T10**	**+ w500**	**+ AOD**
LW HR	0.84	0.84	0.80	**0.79**	0.79	0.79
SW HR	0.51	0.50	0.46	**0.45**	0.45	0.45

As the MAE only provides an average estimation of the quality of the prediction, we also considered the difference between the predicted radiative HRs and those determined from CALIPSO-CloudSat measurements over tropical ocean, separately for Cb, Ci, thin Ci, midlevel and low-level clouds. The LW and SW results of the different experiments, using the testing dataset, are compared in Figure 2. Overall, all results show good agreement between predicted and CALIPSO-CloudSat derived HRs. The differences between mean predicted and 'observed' radiative HRs undulate well around 0 K/day. However, we note that when using the ERA5 vertical velocity at 500 hPa as an additional input variable, the results for Cb and mid- and low-level clouds in the LW are slightly degraded. Similarly, the addition of the monthly mean AOD does not improve the results. This indicates only a medium compatibility between these two variables and the instantaneous AIRS cloud properties and ERA-Interim atmospheric and surface properties. Therefore we use in the following the input variables of experiment 4 for the model development. The 30% quantiles and 70% quantiles of the HR differences in Figure 2 give an indication of the uncertainty, which may be related to differences in horizontal resolution between AIRS and CALIPSO-CloudSat. In particular for convective towers of very large optical depth (Cb) and for mid- and low-level clouds, the coarse AIRS spatial resolution may lead to a mixture of several cloud types or of clouds and clear sky within one footprint.

Furthermore, the radiative HRs also depend on the cloud vertical extent and the number of vertical cloud layers, which are not explicitly given in the input data. However, cloud emissivity and cloud vertical extent are well related (Stubenrauch et al., 2009), as well as cloud vertical extent and number vertical cloud layers (e. g. Wang et al., 2000).

Considering the radiative HR profiles of the different cloud types shown in Figure 3, constructed for one month of data over the whole tropical band (see section 3.3), we find that the largest uncertainties for the relatively high opaque clouds (Cb and Ci), are around the maxima of LW cooling and SW heating which correspond to approximately 15 to 25%. The variability in the vertical profiles of microphysical properties within these clouds which may not be reproduced by the input variables is certainly another cause for these uncertainties.

3.2 Scenes used for the training

When using one model for all clouds over ocean and land, the MAE is 0.82 K/day for LW and 0.51 K/day for SW HRs. Table 3 presents the MAE for the prediction of LW and SW HRs over the testing data, separately for different scene types over ocean and over land. In general, the performance is slightly better over ocean than over land, which can be explained by a greater homogeneity of surface, in particular in the SW, and atmospheric properties. We also observe a decreasing performance from clear sky scenes (LW 0.36 K/day and SW 0.27 K/day) over mid- / low-level clouds towards high-level clouds and Cb, which again can be explained by an increasing inhomogeneity, and in the case of Cb the saturation of ε_{cld} at 1.

We also estimated the uncertainty of the final eight scene-dependent ANN models after having them applied to one month of AIRS data, over the whole tropical band. Regional differences in three atmospheric layers (106-131 hPa, 200-223 hPa, 525-585 hPa) between predicted LW HRs obtained from these models and those from models developed over all clouds, separately over ocean and over land, lie generally within 0.25 K/day, with only a few regions of 0.45 K/day (Figure S5 in the supplement), keeping in mind that the more detailed cloud type distinction will give the better results.

Table 3: MAE (K/d) for the prediction of LW and SW heating rates using models over different scene types.

ocean	clouds	high	Cb	cirrus	mid/low	clear
LW HR	0.79	0.91	1.10	0.90	0.69	0.34
SW HR	0.45	0.62	1.10	0.59	0.33	0.22
land	**clouds**	**high**	**Cb**	**cirrus**	**mid/low**	**clear**
LW HR	0.88	0.99	1.24	0.97	0.67	0.39
SW HR	0.69	0.77	1.35	0.72	0.54	0.36

3.3 Construction of Tropical Heating Rate Fields

After applying the final eight scene-dependent ANN models to one month of AIRS data, over the whole tropical band (30N – 30S) and averaging the resulting radiative HRs at a spatial resolution of 0.5° latitude x 0.5° longitude, we compare the averages of these laterally extended LW and SW HRs with those of FLXHR (along the nadir tracks), separately for clear sky and for five cloud types (Cb, Ci, thin Ci, mid- and low-level clouds). Averages of predicted and 'observed' radiative HRs in Figure 3 are very similar, despite different sampling and spatial resolution. This means that the nadir track statistics gives a good picture on monthly average over the whole tropics and that the prediction models provide on average reliable results. The 30% and 70% quantiles of the distributions indicate variabilities for clear sky and thin cirrus. The larger variabilities for the more opaque clouds are related to their monthly variability in height, optical depth and vertical extent. The relatively large variability for midlevel clouds, with an occurrence in the tropics of about 6%, may be related to the fact that these are often situated in regions with a mixture of different cloud types. The LW HRs are very similar during day and night, and the presented cloud type dependent radiative heating rates agree well with earlier publications (e.g. Oreopoulos et al., 2016).

In a clear sky situation, LW cooling occurs, linked to the absorbed and transmitted energy by the molecules in the atmosphere. As shown in Figure 3, this cooling lies between -2.5 K/day and -2 K/day within the troposphere up to 200 hPa, where it decreases rapidly until it reaches about 0 K/day around 100 hPa. Since the AIRS clear sky identification may also include subvisible cirrus as well as partly cloudy scenes within the AIRS footprint, we estimated how much this affects the radiative HRs by comparing the FLXHR HRs for AIRS clear sky and for CALIPSO-CloudSat clear sky identification (Figure S6 in the supplement). Definitely, there is a slight positive bias in the clear sky LW heating near 100 hPa of about 0.1 to 0.2 K/day due to subvisible cirrus, in particular during night, when the CALIPSO lidar better detects subvisible cirrus. The small SW clear sky heating positive bias of the same order of magnitude between 400 and 800 hPa is most probably linked to contamination by partial cloudiness.

Clouds introduce sharp vertical gradients to this LW cooling: Relatively opaque clouds heat the atmospheric column below by trapping surface emissions, but cool the column above due to excess emission, while thin cirrus heat the UT by intercepting the LW radiation coming from below. Indeed, Figure 3 exhibits a LW cooling above optically thick clouds, the strongest effect above Cb, of about -4.5 K/day around 170 hPa, and a heating within the clouds and below the clouds, compared to clear sky. The small cooling around 550 hPa is due to melting, owing to the transition from ice to liquid phase which occurs at or just below the freezing level at about 5 km altitude throughout the tropics, and the different emissivities of liquid and ice cause a flux divergence at that level (Tristan L'Ecuyer, personal communication). The cooling above mid- and low-level clouds is located around 600 hPa and 800 hPa, respectively. Thin cirrus heat the UT around 100 hPa.

During day in the SW range, the sunlight heats the atmosphere and the particles within the cloud. Figure 3 shows a strong heating in the upper part of the Cb with a maximum of about 8 K/day around 200 hPa, while in the rest of the cloud this effect is negligible, given that the sun is blocked by the dense cloud particles. For midlevel clouds a small peak is found around 600 hPa and for low-level clouds around 850 hPa.

In order to illustrate the additional value of the lateral expansion of the radiative HRs, Figure 4 presents geographical maps of mean LW heating / cooling in four specific pressure layers (around 106, 200, 525 and 850 hPa, respectively) for January 2008, compared to the monthly mean nadir track statistics from CALIPSO-CloudSat. These four pressure layers were chosen according to 1) UT heating by thin cirrus, 2) cooling above Cb and thick cirrus, 3) middle troposphere heating by high thick clouds and 4) cooling above low-level clouds and a heating below clouds. The horizontal structures of the predicted HR fields agree quite well with those from FLXHR, but they appear clearer, since the spare nadir track statistics is quite noisy.

4 The impact of tropical UT cloud systems

By using the 3D radiative heating fields constructed in section 3, we first quantify the effect of tropical clouds on the atmospheric radiative cooling, in comparison to earlier results (section 4.1). In section 4.2 we use the cloud system approach described in section 2.1 to study the heating and cooling within convective cloud systems by distinguishing convective cores (Cb), cirrus anvil (Ci) and surrounding thin cirrus (thin Ci), comparing warm and cool tropical ocean. Finally, we investigate tropical heating changes with respect to variations of tropical surface temperature, climate indices and cloud properties (section 4.3).

4.1 Tropics-wide cloud radiative heating

As seen in Figure 3, clouds introduce sharp vertical gradients to the atmospheric radiative cooling profile, and we are in particular interested in the effect of UT clouds and MCSs. Li et al. (2013) have found that the tropics-wide 24-hr mean UT cloud radiative heating effect has a narrow maximum of about 0.45 K/day around 250 hPa, and that the column-integrated radiative heating of UT clouds accounts for about 20% of the latent heating estimated by TRMM, the latter with a broad peak of about 1.7 K/day around 450 hPa. These results were obtained by using radiative heating rates calculated from ground-based lidar and radar measurements at two ARM sites (Manus and Darwin), classified by ISCCP UT cloud regimes, and then expanded over the deep tropics according to the ISCCP UT cloud regime occurrence frequency.

In order to compare to this significant result, we concentrate on the same latitude band from 15N to 15S and we calculate the 24-hr SW heating rates by multiplying the SW heating rates at 1:30PM LT by 1/(π x cosΘ), where Θ is the solar zenith angle. The latter is about 33° near the equator. Similar to the HR normalisation of Li et al. (2013), we neglect seasonal and geographical variations. The cloud radiative heating effect (CRE) is determined as the difference between cloud HR and clear sky HR, weighted by total cloud amount, and for the CRE of a specific cloud type additionally weighted by its relative amount of specific cloud type. The net CRE is then the sum of the LW CRE, averaged over 1:30AM and 1:30PM LT, and the 24-hr SW CRE using the HRs at 1:30PM LT, weighted by 1/(π x cosΘ), and the whole weighted by the specific cloud amounts averaged over 1:30AM and 1:30PM LT. This estimation assumes that the daily average of cloudiness can be estimated by the values 1:30AM and 1:30PM LT. Indeed, the diurnal variation of UT cloud cover over tropical ocean determined from four daily observations is less than 2% and reaches about 7% over tropical land (Feofilov and Stubenrauch, 2019), with slightly less cirrus and thin cirrus at 1:30PM than at 1:30AM LT.

Total tropical cloud cover is .60%, varying between 57% at 1:30 PM LT and 63% at 1:30 AM LT. We find that 55% of these clouds are UT clouds and 45% are single-layer mid- or low-level clouds. Figure 5 presents a tropics-wide 24 hr – mean radiative heating induced by mid- / low-levels clouds and by UT clouds. The CRE of UT clouds is further distinguished into CRE of MCS and of thin cirrus, and furthermore of thin cirrus associated with MCSs, which are about half of all thin cirrus.

According to Figure 5, the tropics-wide 24 hr – mean CRE of UT clouds is about 0.3 K/day from 250 hPa downward throughout the troposphere. The heating decreases towards 0 K/day at 200 hPa, and above this altitude a small net cooling is observed. Uncertainties related to cloud cover uncertainty and to clear sky identification are also indicated. They have been determined by using the cloud amount at 1:30AM with the HRs at 1:30PM LT and by subtracting the CIRS clear sky identification HR bias (Figure S6 in the supplement). They are small in the lower troposphere, except over land, while they reach up to 0.08 K/day between 450 and 300 hPa.

The CRE values are in the same range as the ones determined by Li et al. (2013). However, the vertical shape of the CRE is significantly different: Whereas the earlier result shows a narrow maximum of 0.45 K/day around 250 hPa and a minimum heating of about 0.1 K/day around 800 hPa, our estimation indicates a much more vertically extended heating effect of 0.3 K/day from 250 hPa downward throughout the troposphere. Compared to Figure 9 of Li et al. (2013), the reinforcement of the latent heating is therefore vertically different, with a larger contribution between 800 hPa and 330 hPa (Figure S6 in the supplement). The enhancement factor between our column-integrated radiative heating of UT clouds and this latent heating (between 100 and 900 hPa) lies between 20 and 25%, very similar and with a slightly larger upper limit than 21% found by Li et al. (2013).

The difference in the profile shape of the UT cloud radiative heating effect is not related to the exploitation of profiles from only two ARM sites, since the profiles averaged over both sites are similar to the ones averaged over the whole tropics (not shown). However, as discussed by Protat et al. (2014), a significant portion of the ice cloud observations using ground-based measurements is attenuated by any liquid cloud below ice clouds or by the liquid part of deep convective systems. This yields a smaller SW heating than the satellite estimates in the middle troposphere. Another key reason for an underestimation of the CRE in the lower troposphere is that the ISCCP cloud regimes have been determined at a spatial resolution of 2.5° and especially the cirrus and mixed cloud regimes, which are the most frequent out of the four UT cloud regimes (72%), include also a certain fraction of single-layer low-level clouds next to the cirrus clouds. When considering the radiative effect of mid- and low-level clouds in Figure 5, which shows a cooling in the middle and lower troposphere down to 880 hPa, the shape of the radiative heating profile contribution of the ISCCP UT cloud regimes can be explained by the fact that at the coarse spatial resolution of 2.5° the UT cloud regimes also contain surrounding single-layer low-level clouds. In addition, the identification of thin cirrus with optical depth less than 1.3, the most frequent within these two ISCCP cloud regimes, is also less reliable, and the cloud height in this case is often just set to the tropopause height (e. g. Stubenrauch et al., 2012).

Further consideration of Figure 5 shows that MCSs considerably contribute to the UT CRE. The UT cooling above the opaque parts of the MCSs is compensated by thin cirrus UT heating, with half of the effect coming from those directly surrounding the anvil and the other half from in situ cirrus. The average net radiative heating within and the cooling above the MCSs seems to be slightly stronger over ocean than over land. Mid- and low-level clouds present a cooling above the clouds and a heating within and below. Since there are more low-level clouds over ocean and more mid-level clouds over land, the shapes of the net CRE differ accordingly. The HR profiles of UT clouds, initially deduced from CALIPSO-CloudSat data, include the effect of lower clouds underneath, as the warming peaks around 920 hPa over ocean and around 650 hPa over land suggest.

From Figure 6, which compares the tropics-wide mean net radiative heating effect of the different cloud types at 1:30 AM LT and at 1:30 PM LT, we deduce a large difference in the profile shapes between nighttime and daytime, and therefore in their vertical heating gradients. During nighttime, UT clouds heat the troposphere from 300 hPa downward increasingly, with a maximum of about 0.6 K/day around 920 hPa. The thicker UT clouds lead to an average cooling, with a minimum of -0.25 K/day around 200 hPa which leads to a strong vertical gradient. The heating of the lower troposphere is slightly larger over land, but with a smaller vertical gradient in the lower troposphere. Thin cirrus show a small average heating effect around 150 hPa, slightly larger over land than over ocean. During daytime, with additional solar heating, UT clouds, in particular the thicker ones, are strongly heated (see also Figure 3), which leads to a tropics-wide maximum of about 0.6 K/day between 250 and 350 hPa. The heating strongly decreases towards the lower troposphere. Again, most of the effect of UT clouds can be explained by MCSs (as both are close to each other).

During nighttime and during daytime, thin cirrus have on average a small heating effect throughout the whole troposphere. The effect of low-level and midlevel clouds differs diurnally: During nighttime they cool the atmosphere above their top, leading to peaks of -0.3 K/day around 820 hPa and of -0.1 K/day around 550 hPa, respectively, and they heat below, while during daytime the SW contribution partly compensates these effects. In general, the UT cloud effect is a strong heating of the UT during daytime and a strong lower tropospheric heating during nighttime, leading to opposite vertical gradients.

Finally, Figure 7 presents geographical maps of precipitable water, surface temperature, frequency of occurrence of UT cloud systems, as well as the 24-hr net CRE, averaged over the whole period of 15 years, in three vertical layers: integrated over 106 to 200 hPa, over 200 to 585 hPa and over 585 to 900 hPa. UT clouds are most frequent over the West Pacific ocean, including Indonesia, over the Amazon region and over Central Africa. These are also the moistest regions. In the uppermost layer we observe horizontal structures linked to thin cirrus heating (red) and to cooling above the thicker parts of the MCSs (blue), whereas regions of clear sky or single layer low-level clouds are in between (yellow to green). Over the West Pacific, the layers underneath are heated by the MCSs, while other regions are cooled just above lower clouds. The horizontal structures agree qualitatively with L'Ecuyer and McGarragh (2010).

4.2 Relation between regional surface temperature and MCSs

A necessary condition for the onset of tropical deep convection, particularly over ocean, is a surface temperature (T_{surf}) above a threshold of about 300 K (e. g. Gray, 1968; Graham and Barnett, 1987, Aumann et al., 2018), though other factors, such as available humidity (which may increase with low-level level convergence), also affect the convective process. Though the shading of the thick anvils may cause some surface cooling during day, slightly offset by the thinner cirrus (Wall et al., 2018), there should be more and deeper MCSs over warm regions than over cool regions. As in a changing climate the extension of warm regions may slightly increase, we compare in this section the properties of MCSs over warmer and over cooler regions.

Recently, Fueglistaler (2019) used the regions of the 30% warmest sea surface temperature (SST) within the tropics as a proxy for regions of deep convective activity. Considering the distributions of the SST underneath the opaque part (cloud emissivity > 0.9) of MCSs and underneath cold MCSs (TCb < 210 K), they are indeed shifted towards warmer SST (Figure S10 in the supplement). We derived the thresholds for the coolest 30% and warmest 30% tropical oceanic regions from ERA-Interim as 300 K and 302 K, respectively. Therefore we use these two thresholds to compare the characteristics of MCSs in cool and in warm oceanic regions.

The tropics-wide 24-hr mean net CRE of the MCSs depends on their frequency of occurrence, their height, horizontal extent and emissivity structure. First we study the effect of the relative occurrence frequency of the different cloud types (mid- / low-level clouds, UT clouds, thin cirrus, MCS and thin cirrus associated with MCS) on the effect of the total CRE. Figure 8 contrasts the CRE of the coolest 30% and warmest 30% ocean regions, for all clouds and when the specific cloud types are present. First of all, over warm regions, clouds, when present, have a heating effect over most of the troposphere, and this heating is mostly driven by MCSs. This is deduced from the strong similarity between the profiles of the present MCSs and those of all clouds. In addition, the UT thin cirrus heating linked to convection is slightly larger than the one of all thin cirrus, which indicates more and slightly thicker thin cirrus linked to convection than those produced in situ. Over cool regions low-level clouds also play an important role, with no heating between 200 and 600 hPa and a strong cooling around 820 hPa.

The influence of emissivity structure is investigated by considering the 24-hr mean net heating / cooling effects of the different parts of the MCSs, convective core, cirrus anvil and surrounding thin cirrus, when MCSs are present. These are presented in Figure 9, for all tropical maritime MCSs and those over cool and warm ocean regions, respectively. As already seen in Figure 3, the shape of the vertical profiles is quite different for the three parts of the MCSs. In the UT (at a height above 200 hPa), we observe an average cooling of about -2 K/day above the convective cores and a much reduced cooling above the cirrus anvil, while the thin cirrus heat the UT by about 0.5 K/day. The troposphere below the height of 200 hPa is strongly heated by the convective cores, much less heated by the cirrus anvils and even less by the surrounding thin cirrus. However, as the convective cores only cover a small fraction of the systems (about 10% on average), the average CRE of the MCSs corresponds to the one of the cirrus anvils. By contrasting cool and warm oceanic regions, the shape of the net radiative heating strengthens the hypothesis of MCSs with larger convective depth above the warm regions, with a cooling of the thicker parts of the MCSs shifted further up into the UT by 50 hPa, while the heating is extended over a broader vertical layer between 550 to 200 hPa. On the other hand, the thin cirrus net radiative heating of the UT of about 0.5 K/day is only associated with the deeper convective systems over the warm regions. These are mostly large MCSs with multiple convective cores.

Figure 10 compares the properties of these maritime MCSs over cool and warm regions. In general, the warm regions are more humid according to the distributions of total precipitable water from ERA-Interim (not shown) and present also slightly more humidity in the upper troposphere (last panel of Figure 10). The distributions in Figure 10 indicate that maritime MCSs overlying warm regions have colder convective cores (given by their near cloud top temperature TCb), which means that they are extending higher into the troposphere, and have also more often a larger horizontal extent (MCS radius of convective core and cirrus anvil), in agreement with a regional study by Horvath and Soden (2008). The area occupied by thin cirrus associated with MCS, relative to the anvil area, is also larger. This can be explained by i) a larger relative humidity at higher altitude and ii) additional UT humidification originating from the convection (e. g. Luo et al., 2011). When convective systems are present over the cool regions, they seem to be more confined, consisting more often of systems with one single convective core (nb(singleCore MCS)/nb(MCS) close to 1), with a slightly larger average emissivity (MCS emissivity: averaged over convective cores and cirrus anvil). The latter is in agreement with a study of Del Genio et al. (2005), which revealed a decreasing detrainment and increasing precipitation efficiency within maritime MCSs when the underlying SST increases.

As mentioned at the beginning of this section, not only SST, but also other factors influence the properties of the MCSs. Therefore we also investigated the heating effects of the different parts of the MCSs over the tropical Atlantic, East Pacific, Central Pacific and West Pacific (Figure S11 in the supplement), with mean SST increasing from Atlantic towards West Pacific. Though differences in dynamics and atmospheric environment between these regions certainly also play a role (e. g. Henderson et al., 2018), the differences in the 24-hr net radiative heating effect are larger between cool and warm periods within these regions than between these regions. From this one may conclude that the on average slightly increasing CRE of the MCSs from tropical Atlantic to West Pacific can be mostly explained by increasing parts of warm SSTs from the tropical Atlantic towards the West Pacific.

4.3 Changes in tropical heating and in MCSs in dependence of tropical surface temperature anomaly

In section 4.2 we have shown that the heating over the warmer tropical ocean regions is mostly influenced by MCSs and that the MCSs in these warmer regions also have a larger convective depth and are slightly larger, but with slightly smaller emissivity, than in the cooler regions. As we have built 15 years of HR fields and of MCS properties, we investigate in this section interannual variations in MCSs and in resulting atmospheric heating / cooling and try to relate these to tropical T_{surf} anomalies and to phenomena which influence the interannual variability. Even if the time period covered by AIRS observations may still not be long enough for climate change attribution, we note that the tropical T_{surf} anomalies from ERA-Interim are very well correlated with global T_{surf} anomalies (GISTEMP v4, Lenssen et al., 2019), with a Pearson correlation coefficient r of 0.91.

The mesoscale UT cloud systems cover 25.6% of the tropical latitude band, with 80% of their coverage from MCSs (at least one convective core) and 6% from thin cirrus systems. Moreover 48% of the MCSs are cold MCSs with near-cloud-top temperature TCb < 210 K. We estimate changes in the properties of the tropical MCSs in relation with tropical surface warming by determining linear regression slopes between the anomalies of the MCS properties and the tropical T_{surf} anomalies, after smoothing the deseasonalized data by 12-month running means. This is a common method (e. g. Liu et al., 2017; Stubenrauch et al., 2017), and uncertainties are derived from the residuals of the linear regression. Time series are presented in Figures 11 to Figure 13.

The tropical T_{surf} anomalies are related to the El-Niño-Southern Oscillation (ENSO) and to the Inter-decadal Pacific Oscillation (PDO), both with r = 0.71, PDO being influenced by ENSO (r = 0.75). The Oceanic Niño Index (ONI) and the NCEI PDO index are provided by the National Oceanic and Atmospheric Administration (NOAA. El Niño (La Niña) events are linked to a positive (negative) tropical T_{surf} anomaly. Their initiation is given by a local SST anomaly in the tropical Pacific, which then changes the east-west SST gradient, affecting the atmospheric circulation and the distribution of clouds. These phenomena have been extensively studied (e. g. Schumacher et al., 2004; Su and Jiang, 2013; Stephens et al., 2018b; Sullivan et al., 2019). The coverage of all clouds, of low-level clouds, of UT clouds and of MCS is stable over the whole period, with undulations of less than 0.01. While low-level and UT cloud cover show no significant correlations with anomalies of tropical T_{surf}, ONI and PDO, total cloud cover and relative MCS cover show slight anti-correlations with ONI (r=0.62 and r=0.74, respectively), and the latter shows a very small decrease of -2 ± 1 % /K (r=0.7). On the other hand, we notice that MCSs get colder (deeper) with T_{surf} warming (convective core near top temperature decreasing by – 3.4 ± 0.2 K/K with r = 0.78), and thus the surrounding thin cirrus area relative to the anvil area slightly increases by +12 ± 1%/K, with r = 0.85. When considering the coverage of cold MCSs relative to all MCSs, it increases by 13.2 ± 1.3 %/K, but this correlation is more uncertain (r = 0.60). Yet, it is interesting to note that the coverage of cold MCS seems to be lagged to the convective core temperature.

The CRE of MCSs is influenced by their depth as well as by their coverage. When comparing the oscillations of MCS coverage anomalies to those of cold MCS coverage anomalies, they seem to be slightly anti-correlated, so that there are phases when convective systems are deeper (colder) and the relative coverage of MCS is reduced. This is in agreement with Zelinka and Hartmann (2010), who found during El Niño periods a decrease of high-level cloud amount as well as an increase in their height.

The time series of the anomalies of the 24-hr net vertically resolved heating / cooling effects of MCSs shown in Figure 12 reveal vertical dipole effects, which seem to be linked to ENSO variability and can be explained by changes in convective depth of the MCSs. The anomalies have values of about -0.4 K/day and +0.4 K/day, respectively. Figure 12 also presents the time series of the anomalies of the 24-hr net vertically resolved heating / cooling effects of all clouds, when present, and of all clouds, weighted by their cover, all averaged over the latitude band 30N to 30S. The anomalies in the upper and middle troposphere have similar patterns as the ones for the MCSs, only much smaller in magnitude, because their relative frequency of occurrence is taken into account. We also observe strong cooling and heating anomaly patterns in the lower atmosphere, linked to the occurrence of stratocumulus and stratus cloud fields. There is evidence of a cooling in the atmospheric boundary layer (linked to low-level clouds) is associated with warming in the upper and middle troposphere (linked to MCS activity), just balancing the opposite effects in warm and cool regions (see Figure 8). In order to quantify the suggested correlations, we averaged these CRE anomalies over three atmospheric layers (100-200 hPa, 200–650 hPa and 650–900 hPa) and analysed correlations between them and the variables displayed in Figure 11. Figure 13 displays the time series of the CRE anomalies in these three layers for MCS and for all clouds weighted by their coverage, as well as the latter in the 650-900 hPa layer over the cool regions (T_{surf} < 300 K). Considering MCS, we observe the above-mentioned dipole effect between the 100-200 hPa and the 200-650 hPa layers, with slightly more cooling near the tropopause when more heating in the atmosphere below, thus increasing the vertical gradients, during periods of warmer T_{surf} (El Niño). Deeper MCSs correspond to a stronger heating in the 200-650 hPa layer (correlation with TCb : r = 0.80). The correlations with T_{surf} and ONI anomalies have values equal to 0.69 and 0.57, respectively, keeping in mind that ONI is an oceanic phenomenon and we compare to the HR anomalies of the whole tropics. When considering all clouds and all scenes, we find an interesting correlation between the CRE anomalies in the layer close to the tropopause and those of Tsurf (r = 0.83 and r = 0.86, respectively), suggesting a slight heating with warmer T_{surf}, which is mostly due to more thin cirrus surrounding the anvils (r = 0.70).

Finally, our hypothesis of an energetic connection between the convective regions and the subsidence regions, can be consolidated by a correlation coefficient between the MCS heating in the 200-650 hPa layer (red broken line in Figure 13) and the cooling in the 650-900 hPa layer of the cool regions (green dotted line in Figure 13), with a value equal to 0.71. This confirms that within the tropics and subtropics the extent of the stratocumulus and stratus fields is energetically constrained by the height and extent of MCSs (e.g. Hang et al., 2019; Jakob et al., 2019). Based on these results it would be interesting to study in more detail possible lags in the time series at a finer time scale. A first study by Fueglistaler (2019) has shown transitions from an initial decrease in oceanic cloudiness due to lagged warming of the warmest waters to increased cloudiness in the decay phase of El Niño.

5 Conclusions and Outlook

Radiative HR profiles can be derived using the active lidar and radar measurements from CALIPSO and CloudSat, but only on narrow nadir tracks. On the other hand, AIRS, also part of the A-Train satellite constellation, provides cloud properties with a large instantaneous horizontal coverage. We constructed 3D HR fields within 30N to 30S, for the period 2003 to 2018 by using these radiative HRs for the training and applying the resulting ANN models on cloud properties from AIRS and atmospheric and surface properties from ECMWF meteorological reanalyses.

We demonstrated that non-linear ANN regression models, trained on large statistics of four years of collocated data, are appropriate methods to estimate tropical radiative HRs from about 40 cloud, atmospheric and surface properties. Column-integrated MAE is about 0.8 K/day (0.5 K/day) for cloudy scenes and 0.4 K/day (0.3 K/day) for clear sky in the LW (SW). Separate models for i) Cb, ii) cirrus and thin cirrus, iii) mid- and low-level clouds and iv) clear sky, independently over ocean and over land, perform slightly better, with mean predicted radiative HRs very close to the 'observed' ones, with uncertainties within 0.25 K/day per layer. The improvement is most noticeable for Cb, with uncertainties around the maxima of LW cooling and SW heating due to small vertical shifts in the HR profiles. The monthly mean horizontal structures of the predicted HR fields agree well with the original ones from CALIPSO-CloudSat, but they appear more clearly, due to the lateral expansion.

We have produced the longest tropical HR dataset available by applying the ANN models to 15 years of combined AIRS and ECMWF data. By studying the long-term temporal behaviour of the HRs, in particular in relation to tropical T_{surf} variability, we have demonstrated that the regression models produce also reliable results outside the training period (assuming a non-changing relationship between the input parameters and the HRs).

We confirm that most of the total cloud net radiative heating effect in the deep tropics (15N-15S) comes from UT clouds. These clouds have a 24-hr mean net radiative heating effect of about 0.3 K/day from 250 hPa downward, enhancing the column-integrated latent heating by 22% ± 3%. This value is only slightly larger than earlier results of about 20% (Li et al., 2013), using ISCCP cloud data, but our result may still be slightly underestimated, because of the cloud contamination of the clear sky scenes identified by AIRS and the slightly underestimated LW warming above 12 km in the original FLXHR-LIDAR (R04) data linked to cirrus microphysical assumptions. Yet, the shape of the heating profiles compared to those of Li et al. (2013) is significantly different, with our estimation indicating a much more vertically extended heating. This suggests an underestimation of the heating in the middle troposphere of the earlier result, which can be explained by the shading effect of underlying low-level clouds on ground-based measurements and by a mixture of cirrus and surrounding single-layer low-level clouds linked to a coarse spatial resolution of the cloud regime approach.

In general, the UT cloud effect is a strong heating of the UT during daytime and a strong lower tropospheric heating during nighttime, leading to opposite diurnal vertical gradients. The heating profile shapes of the convective cores, cirrus anvil and surrounding thin cirrus of MCS differ significantly: The troposphere from 200 hPa downward is strongly heated by the convective cores, less heated by the cirrus anvils and even less by the surrounding thin cirrus. However, as the convective cores only cover a small fraction of the systems, the average heating effect of the MCSs corresponds to the one of the cirrus anvils.

Over the warmest 30% ocean regions, the heating is mostly driven by MCSs, which also have a larger convective depth than the ones over the coolest 30% ocean regions. The consequence is a heating over a broader vertical layer, between 550 to 200 hPa. The thin cirrus linked to the MCSs in these regions heat the UT by about 0.5 K/day, more than the in situ formed cirrus. The latter play a more important role over cool regions, as well as mid- and low-level clouds (over ocean), with much less heating between 200 and 900 hPa.

During the time period 2003 to 2018, the coverage of all clouds, UT clouds, low clouds and MCS is relatively stable, with undulations less than 1%. On the other hand, MCSs get colder (deeper) with tropical T_{surf} warming (by – 3.4 ± 0.2 K/K), and thus the surrounding thin cirrus area relative to the anvil area slightly increases by +12 ± 1%/K.

The time series of the anomalies of the 24-hr net vertical heating / cooling effects of clouds and in particular of the MCSs exhibits vertical dipole effects, related to tropical T_{surf} variability and explained by changes in convective depth of the MCSs: During periods of warmer tropical T_{surf} (El Niño), the HR vertical structure anomaly suggests deeper MCS, with vertically broader heating. The data also reveal a small heating effect in the layer close the tropopause with tropical surface warming, mostly due to more thin cirrus surrounding the anvils of the MCSs. Finally, we highlighted a correlation of the MCS heating in the upper and middle troposphere and the (low-level) cloud cooling in the lower atmosphere in the cool regions (r=0.72). This shows, in agreement with other studies, that within the tropics and subtropics the extent of the low-level cloud fields is energetically constrained by the height and extent of the MCSs. Lags between the different variables in the time series will be further explored at a finer time scale.

The new data base of the radiative heating rate fields builds the basis for future studies. Therefore, we will add the latent heating profiles derived from the Tropical Rainfall Measuring Mission (TRMM) to this synergistic data set, which provides for the first time a 3D view of the radiative heating profiles over a long time period. As the coincidences in time with AIRS are small, we will use again machine learning techniques, similar to the ones described in this article. This data base of UT cloud systems is being constructed within the framework of the GEWEX (Global Energy and Water Exchanges) Process Evaluation Study on Upper Tropospheric Clouds and Convection (GEWEX UTCC PROES, https://gewex-utcc-proes.aeris-data.fr/) to advance our knowledge on the climate feedbacks of UT clouds. In general, climate feedback studies are undertaken by climate model simulations, which rely upon their representation of convection and detrainment. The cloud system approach has already proved its usefulness in the evaluation of a new bulk ice cloud scheme in the LMD GCM (Stubenrauch et al., 2019), and the HRs may be used to distinguish between parameterizations of ice cloud radiative properties. Furthermore, this data base, in particular when including the total 3D diabatic heating, will be used to quantify the dynamical response of the climate system to the atmospheric heating induced by the anvil cirrus, refining and extending the studies of Schumacher et al.(2004) and Li et al. (2013).

In the future we will train the ANN models again with the improved version of the FLXHR-LIDAR data and a new version of the CIRS data (using ERA5 ancillary data, as ERA-Interim data production ceased in August 2019).

6 Acknowledgements and Data

This work is supported by the Centre National de la Recherche Scientifique (CNRS) and the Centre National d'Etudes Spatiales (CNES). The authors thank the members of the AIRS, CALIPSO and CloudSat science teams for their efforts and cooperation in providing the data, as well as the engineers and space agencies who control the data quality. AIRS CIRS data have been produced by the French Data Centre AERIS and are distributed at https://cirs.aeris-data.fr. In section 4.3, we used global T_{surf} anomalies derived by the GISTEMP Team, (2020). The dataset was accessed in 2019 at https:// data.giss.nasa.gov/gistemp/. Monthly indices of ENSO strength (ONI) and of PDO were obtained from NOAA (https://origin.cpc.ncep.noaa.gov/products/analysis_monitoring/ensostuff/detrend.nino34.ascii.txt and https://www.ncdc. noaa.gov/teleconnections/pdo/, respectively).

References

Ackerman, T. P., Liou, K.-N., Valero, F. P. J., and Pfister, L.: Heating Rates in Tropical Anvils, J. Atmos. Sci., 45, 1606-1623, https://doi.org/ 10.1175/1520-0469(1988)045<1606:HRITA>2.0.CO;2, 1988.

Aumann, H. H., Behrangi, A., and Wang, Y.: Increased Frequency of Extreme Tropical Deep Convection: AIRS Observations and Climate Model Predictions, Geophys. Res. Lett., 45, 13530-13537, https://doi.org/10.1029/2018GL079423, 2018.

Bergman, J. W., and Hendon, H. H.: Cloud Radiative Forcing of the Low-Latitude Tropospheric Circulation: Linear Calculations, J. Atmos. Sci., 57, 2225-2245, https://doi.org/10.1175/1520-0469(2000)057<2225:CRFOTL>2.0.CO;2, 2000.

Boucher, O., D. Randall, P. Artaxo, C. Bretherton, G. Feingold, P. Forster, V.-M. Kerminen, Y. Kondo, H. Liao, U. Lohmann, P. Rasch, S.K. Satheesh, S. Sherwood, B. Stevens, and X.Y. Zhang, Clouds and aerosols. In Climate Change 2013: The Physical Science Basis. Contribution of Working Group I to the Fifth Assessment Report of the Intergovernmental Panel on Climate Change. T.F. Stocker, D. Qin, G.-K. Plattner, M. Tignor, S.K. Allen, J. Doschung, A. Nauels, Y. Xia, V. Bex, and P.M. Midgley, Eds. Cambridge University Press, 571-657, https://doi.org/10.1017/CBO9781107415324.01, 2013.

Chahine, M. T., Pagano, T. S., Aumann, H. H., Atlas, R., Barnet, C., Blaisdell, J., Chen, L., Divakarla, M., Fetzer, E. J., Goldberg, M., Gautier, C., Granger, S., Hannon, S., Irion, F. W., Kakar, R., Kalnay, E., Lambrigtsen, B. H., Lee, S., Le Marshall, J., McMillan, W. W., McMillin, L., Olsen, E. T., Revercomb, H., Rosenkranz, P., Smith,W. L., Staelin, D., Strow, L. L., Susskind, J., Tobin, D., Wolf, W., and Zhou, L.: AIRS: Improving weather forecasting and providing new data on greenhouse gases, Bull. Amer. Meteor. Soc., 87, 911-926, https://doi.org/10.1175/BAMS-87-7-911, 2006.

Chédin, A., Serrar, S., Scott, N. A., Crevoisier, C., and Armante, R.: First global measurement of midtropospheric CO_2 from NOAA polar satellites: Tropical zone, J. Geophys. Res., 108, https://doi.org/101029/2003JD003439, 2003.

Dee, D. P., Uppala, S. M., Simmons, A. J., Berrisford, P., Poli, P., Kobayashi, S., Andrae, U., Balmaseda, M. A., Balsamo, G., Bauer, P., Bechtold, P., Beljaars, A. C. M., van de Berg, L., Bidlot, J., Bormann, N., Delsol, C., Dragani, R., Fuentes, M., Geer, A. J., Haimberger, L., Healy, S. B., Hersbach, H., Holm, E. V., Isaksen, L., Kallberg, P., Kohler, M., Matricardi, M., McNally, A. P., Monge-Sanz, B. M., Morcrette, J.-J., Park, B.-K., Peubey, C., de Rosnay, P., Tavolato, C., Thepaut, J.-N., and Vitart, F.: The ERA-Interim reanalysis: configuration and performance of the data assimilation system, Q. J. R. Meteorol. Soc., 137, 553–597, https://doi.org/10.1002/qj.828, 2011.

Del Genio, A.D., W. Kovari, M.-S. Yao, and J. Jonas: Cumulus microphysics and climate sensitivity. *J. Climate*, 18, 2376-2387, https://doi.org/10.1175/JCLI3413.1, 2005.

Deng M, Mace, G. G., Wang, Z., and Lawson, R. P.: Evaluation of Several A-Train Ice Cloud Retrieval Products with In Situ Measurements Collected during the SPARTICUS Campaign. J. Appl. Meteor. Climatol., 52, 1014–1030, https://doi.org/10.1175/JAMC-D-12-054.1, 2013.

Feofilov, A. G., Stubenrauch, C. J., and Delanoë, J.: Ice water content vertical profiles of high-level clouds: classification and impact on radiative fluxes, Atmos. Chem. Phys., 15, 12327–12344, https://doi.org/10.5194/acp-15-12327-2015, 2015.

Feofilov, A. G. and Stubenrauch, C. J., Diurnal variation of high-level clouds from the synergy of AIRS and IASI space-borne infrared sounders, Atmos. Chem. Phys., 19, 13957-13972, https://doi.org/10.5194/acp-19-13957-2019, 2019.

Fueglistaler, S.: Observational Evidence for Two Modes of Coupling Between Sea Surface Temperatures, Tropospheric Temperature Profile, and Shortwave Cloud Radiative Effect in the Tropics, Geophys. Res. Lett., 46, 9890-9898, https://doi.org/10.1029/2019GL083990, 2019.

Guignard, A., Stubenrauch, C. J., Baran, A. J., and Armante, R.: Bulk microphysical properties of semi-transparent cirrus from AIRS: a six year global climatology and statistical analysis in synergy with geometrical profiling data from CloudSat-CALIPSO, Atmos. Chem. Phys., 12, 503–525, https://doi.org/10.5194/acp-12-503-2012, 2012.

Graham, N. E., and Barnett, T. P.: Sea Surface Temperature, Surface Wind Divergence, and Convection over Tropical Oceans, Science, 238(4827):657-9, https//doi.org/10.1126/science.238.4827.657, 1987.

Gray, W.: A global view of the origin of tropical disturbances and storms, Mon. Weath. Rev., 96, 669-700, https://doi.org/10.1175/1520-0493(1968)096<0669:GVOTOO>2.0.CO;2, 1968.

Ham, S.-H., Kato, S., Rose, F. G., Winker, D., L'Ecuyer, T., Mace, G. G., Painemal, D., Sun-Mack, S, Chen, Y., and Miller W. F.: Cloud occurrences and cloudradiative effects (CREs) fromCERES-CALIPSO-CloudSat-MODIS (CCCM) and CloudSat radar-lidar (RL) products, J. Geophys. Res. Atmos., 122, 8852–8884, https://doi.org/10.1002/2017JD026725, 2017.

Hang, Y., L'Ecuyer, T. S., Henderson, D. S., Matus, A. V., and Wang, Z.: Reassessing the Effect of Cloud Type on Earth's Energy Balance in the Age of Active Spaceborne Observations. Part II: Atmospheric Heating. J. Climate, 32, 6219–6236, https://doi.org/10.1175/JCLI-D-18-0754.1, 2019.

Haynes, J. M., L'Ecuyer, T., Stephens, G. L., Miller, S. D., Mitrescu, C., Wood, N. B., and Tanelli, S.: Rainfall retrieval over the ocean with spacenorne W-band radar, J. Geophys. Res. Atmospheres, 114, D00A22, https://doi.org/10.1029/2008JD009973, 2009.

Henderson, D. S., L'Ecuyer, T., Stephens, G. L, Partain, P., and Sekiguchi, M.: A Multisensor Perspective on the Radiative Impacts of Clouds and Aerosols, J. Appl. Meteor. Climatol., 52, 853–871, https://doi.org/10.1175/JAMC-D-12-025.1, 2013.

Hersbach, H., and coauthors: The ERA5 Global Reanalysis, Quarterly J. Roy. Meteor. Soc., https://doi.org/10.1002/qj.3803, 2020.

Horvath, A., and Soden, B. J., Lagrangian diagnostics of tropical deep convection and its effect upon upper-tropospheric humidity. J. Climate, 21, 1013-1028. https://doi.org/10.1175/2007JCLI1786.1, 2008.

Houze, R. A. Jr., Mesoscale convective systems, Rev. Geophys., 42, RG4003, https://doi.org/10.1029/2004RG000150, 2004.

Igel, M. R., Drager, A. J., and Van Den Heever, S. C.: A CloudSat cloud object partitioning technique and assessment and integration of deep convective anvil sensitivities to sea surface temperature, J. Geophys. Res., 119, 10515-10535, https://doi.org/10.1002/2014JD021717, 2014.

Jakob, C., Singh, M. S., and Jungandreas, L.: Radiative convective equilibrium and organized convection: An observational perspective. J. Geophys. Res. Atmospheres, 124, 5418–5430. https://doi.org/10.1029/2018JD030092, 2019.

Johansson, E., Devasthale, A., L'Ecuyer, T., Ekman, A. M. L., and Tjernström, M.: The vertical structure of cloud radiative heating over the Indian subcontinent during summer monsoon, Atmos. Chem. Phys., 15, 11557–11570, https://doi.org/10.5194/acp-15-11557-2015, 2015.

Kingma, D. P., and Ba, J., Adam: A Method for Stochastic Optimization, 3rd Int. Conf. for Learning Representations, San, Diego, 2015, arXiv: 1412.6980, 2014.

Kleynhans, T., Montanaro, M., Gerace, A., and Kanan, C.: Predicting Top-of-Atmosphere Thermal Radiance Using MERRA-2 Atmospheric Data with Deep Learning. Remote Sens., 9, 1133, https://doi.org/10.3390/rs9111133, 2017.

Lenssen, N., Schmidt, G., Hansen, J., Menne, M., Persin, A., Ruedy, R., and Zyss, D., Improvements in the GISTEMP uncertainty model. J. Geophys. Res. Atmos., 124, 12, 6307-6326, https://doi.org/10.1029/2018JD029522, 2019.

Levy, R., Remer, L., Tanré, D., Mattoo, S., and Kaufman, Y.: Algorithm for remote sensing of tropospheric aerosol over dark targets from MODIS: Collections 005 and 051: Revision 2, MODIS Algorithm Theoretical Basis Document, 2009.Roca, R., Aublanc, J., Chambon, P., Fiolleau, T., and Viltard, N.: Robust Observational Quantification of the Contribution of Mesoscale Convective Systems to Rainfall in the Tropics. J. Climate, 27, 4952–4958, https://doi.org/10.1175/JCLI-D-13-00628.1, 2014.

L'Ecuyer, T., and McGarragh, G.: A 10-Year Climatology of Tropical Radiative Heating and Its Vertical Structure from TRMM Observations, J. Climate 23 (3): 519–541, https://doi.org/10.1175/2009JCLI3018.1, 2010.

Li, W., Schumacher, C., and McFarlane, S. A.: Radiative heating of the ISCCP upper level cloud regimes and its impact on the large-scale tropical circulation, J. Geophys. Res. Atmos., 118, 592–604, https://doi.org/10.1002/jgrd.50114, 2013.

Luo, Z., and Rossow, W.B.: Characterizing tropical cirrus life cycle, evolution, and interaction with upper-tropospheric water vapor using Lagrangian trajectory analysis of satellite observations. J. Climate, 17, 4541-4563, https://doi.org/10.1175/3222.1, 2004.

Luo, Z., Kley, D., Johnson, R. H., Liu, G. Y., Nawrath, S., and Smit, H. G. J.: Influence of Sea Surface Temperature on Humidity and Temperature in the Outflow of Tropical Deep Convection, J. Climate, 25, 1340-1348, https://doi.org/ 10.1175/2011JCLI4124.1, 2011.

Mace, G. G., Zhang, Q., Vaughan, M., Marchand, R., Stephens, G., Trepte, C., and Winker, D.: A description of hydrometeor layer occurrence statistics derived from the first year of merged Cloudsat and CALIPSO data, J. Geophys. Res., 114, D00A26, https://doi.org/10.1029/2007JD009755, 2009.

Matus, A. ,and LEcuyer, T.S.: The role of cloud phase in Earth's radiation budget. J. Geophys. Res. Atmos., 122, 2559-2578, https://doi.org/10.1002/2016JD025951, 2017.

Oreopoulos, L., Cho, N., Lee, D., and Kato, S.: Radiative effects of global MODIS cloud regimes, J. Geophys. Res. Atmos., 121, 2299–2317, https://doi.org/10.1002/2015JD024502, 2016.

Paul, M., Aires, F., Prigent, C., Trigo, I., and Bernardo, F.: An innovative physical scheme to retrieve simultaneously surface temperature and emissivities using high spectral infrared observations from IASI. J. Geophys. Res., 117, D11302, https://doi.org/10.1029/2011JD017296, 2012.

Protat, A., Young, S.A. McFarlane, S.A., L'Ecuyer, T., Mace, G.G., Comstock, J.M., Long, C.N., Berry, E., and Delanoë, J.: Reconciling Ground-Based and Space-Based Estimates of the Frequency of Occurrence and Radiative Effect of Clouds around Darwin, Australia, J. Appl. Meteor. Climatol., 53, 456–478, https://doi.org/10.1175/JAMC-D-13-072.1, 2014.

Protopapadaki, E.-S., Stubenrauch, C. J., and Feofilov, A. G.: Upper Tropospheric cloud Systems derived from IR Sounders: Properties of Cirrus Anvils in the Tropics, Atmosph. Chem. Phys., 17, 3845-3859, https://doi.org/10.5194/acp-17-3845-2017, 2017.

Ritter, B., and Geleyn, J.-F.: A comprehensive radiation scheme for numerical weather prediction models with potential applications in climate simulations. Mon. Wea. Rev., 120, 303–325, https://doi.org/10.1175/1520-0493(1992)120<0303:ACRSFN>2.0.CO;2, 1992.

Schumacher, C., Houze, R. A., and Kraucunas, I., The Tropical Dynamical Response to Latent Heating Estimates Derived from the TRMM Precipitation Radar, J. Atmos. Sci., 61, 1341-1358, https://doi.org/10.1175/1520-0469(2004)061<1341 :TTDRTL>2.0.CO;2, 2004.

Sherwood, S. C., Ramanathan, V., Barnett, T., Tyree, M., and Roeckner, E.: Response of an atmospheric GCM to radiative forcing of tropical clouds. J. Geophys. Res., 99**,** 20 829–20 845, https://doi.org/10.1002/qj.49711448209, 1994.

Slingo, J. M., and Slingo, A.: The response of a general circulation model to cloud longwave radiative forcing. II: Further studies, Quart. J. Roy. Meteor. Soc., 117, 333–364, https://doi.org/10.1002/qj.49711448209, 1991.

Snauffer, A. M., Hsieh, W. W., Cannon, A. J., and Schnorbus, M. A.: Improving gridded snow water equivalent products in British Columbia, Canada: multi-source data fusion by neural network models, The Cryosphere, 12, 891-905, https://doi.org/10.5194/tc-12-891-2018, 2018.

Sohn, B.-J.: Cloud-Induced Infrared Radiative Heating and Its Implications for Large-Scale Tropical Circulations, J. Atmos. Sci., 56, 2657-2672, https://doi.org/10.1175/1520-0469(1999)056<2657:CIIRHA>2.0.CO;2, 1999.

Stein, T. H. M., Holloway, C. E., Tobin, I., and Bony, S.: Observed relationships between cloud vertical structure and convective aggregation over tropical ocean. J. Climate, 30, 2187–2207, https://doi.org/10.1175/JCLI-D-16-0125.1, 2017.

Stephens, G. L., and Webster, P. J. : Cloud decoupling of surface and planetary radiative budgets. J. Atmos. Sci., 41, 681–686, https://doi.org/ 10.1175/1520-0469(1984)041<0681:CDOTSA>2.0.CO;2, 1984.

Stephens, G. L., Webster, P. J., Johnson, R. H., Engelen, R., and L'Ecuyer, T. : Observational Evidence for the Mutual Regulation of the Tropical Hydrological Cycle and Tropical Sea Surface Temperatures, J. Climate, 17, 2213-2224, https://doi.org/10.1175/1520-0442(2004)017<2213:OEFTMR>2.0.CO;2, 2004.

Stephens, G. L, Van den Heever, S., and Pakula, L. A.: Radiative Convective Feedback in Idealized States of Radiative-Convective Equilibrium. J. Atmos. Sci., 65, 3899-3916, https://doi.org/10.1175/2008JAS2524.1, 2008.

Stephens, G. L., Winker, D., Pelon, J., Trepte, C., Vane, D. G, .Yuhas, C., L'Ecuyer, T., and Lebsock, M.: CloudSat and CALIPSO within the A-Train: Ten Years of Actively Observing the Earth System. Bull. Amer. Meteorol. Soc., 83, 1771-1790, https://doi.org/10.1175/BAMS-D-16-0324.1, 2018a.

Stephens, G.L., Hakuba, M.Z., Webb, M., Lebsock, M., Yue, Q., Kahn, B.H., Hristova-Veleva, S., Rapp, A., Stubenrauch, C., Elsaesser, G.S., and Slingo, J.: Regional intensification of the tropical hydrological cycle during ENSO. Geophys. Res. Lett., 45, 4361-4370, doi:10.1029/2018GL077598, 2018b.

Strahler, A. H., Muller, J.-P., and MODIS Science Team Members: MODIS BRDF/Albedo Product: Algorithm Theoretical Basis Document Version 5.0, MODIS Product ID: ATBD-MOD-43, 1999.

Stubenrauch, C. J., Chédin, A., Armante, R. and Scott, N. A.: Clouds as Seen by Satellite Sounders (3I) and Imagers (ISCCP): II) A New Approach for Cloud Parameter Determination in the 3I Algorithms, J. Climate, 12, 2214-2223, https://doi.org/10.1175/1520-0442(1999)012<2214:CASBSS>2.0.CO;2, 1999.

Stubenrauch, C. J., Rossow, W. B., Kinne, S., Ackerman, S., Cesana, G., Chepfer, H., Di Girolamo, L., Getzewich, B., Guignard, A., Heidinger, A., Maddux, B., Menzel, P., Minnis, P., Pearl, C., Platnick, S., Poulsen, C., Riedi, J., Sun-Mack, S., Walther, A., Winker, D., Zeng, S., Zhao, G.: Assessment of Global Cloud Datasets from Satellites: Project and Database initiated by the GEWEX Radiation Panel, Bull. Amer. Meteor. Soc., https://doi.org/10.1175/BAMS-D-12-00117.1, 2013.

Stubenrauch, C. J., Feofilov, A. G., Protopapadaki, E.-S., & Armante, R.: Cloud climatologies from the InfraRed Sounders AIRS and IASI: Strengths and Applications, Atmosph. Chem. Phys., 17, 13625-13644, https://doi.org/10.5194/acp-17-13625-2017, 2017.

Stubenrauch, C. J., Bonazzola, M., Protopapadaki, S. E., and Musat, I., New cloud system metrics to assess bulk ice cloud schemes in a GCM. J. Advances in Modeling Earth Systems, 11, https://doi.org/10.1029/2019MS001642, 2019.

Su, H., and Jiang, J. H., Tropical Clouds and Circulation Changes During the 2006-07 and 2009-10 El Niños, J. Climate, 26, 399–413, https://doi.org/10.1175/JCLI-D-12-00152.1, 2013.

Sullivan, S. C., Schiro, K. A., Stubenrauch, C., and Gentine, P.: The Response of Tropical Organized Convection to El Niño Warming, J. Geophys. Res. Atmos., 124 https://doi.org/10.1029/2019JD031026, 2019.

Tan, J., Jakob, C., Rossow, W.B. and Tselioudis, G.: The role of organized deep convection in explaining observed tropical rainfall changes. Nature, 519, 451-454, https://doi.org/10.1038/nature14339, 2015.

Tselioudis, G., Rossow, W. B., Zhang, Y., and Konsta, D.: Global Weather States and Their Properties from Passive and Active Satellite Cloud Retrievals, J. Climate, 26, 7734-7746, https://doi.org/10.1175/JCLI-D-13-00024.1, 2013.

Wall, C. J., Hartmann, D. L., Thieman, M. M., Smith, W. L., and Minnis, P.: The life cycle of anvil clouds and the top-of-atmosphere radiation balance over the tropical West Pacific. J. Climate, 31, 10,059– 10,080. https://doi.org/10.1175/JCLI-D-18-0154.1, 2018.

Wang, J., Rossow,W. B., and Zhang, Y.: Cloud Vertical Structure and its Variations from a 20-Yr Global Rawinsonde Dataset. J. Climate, 13, 3041-3056, https:// doi.org/10.1175/1520-0442(2000)013<3041:CVSAIV>2.0.CO;2, 2000.

Wu, X. and Smith, W. L.: Emissivity of rough sea surface for 8 –13 μm: modelling and verification, Appl. Optics, 36, 2609–2619, https://doi.org/10.1364/AO.36.002609, 1997.

Yuan, J., and Houze Jr, R. A.: Global Variability of Mesoscale Convective System Anvil Structure from A-Train Satellite Data, J. Climate, 23, 5864-5888, https://doi.org/10.1175/2010JCLI3671.1, 2010.

Zelinka, M. D., and Hartmann, D. L.: Why is longwave cloud feedback positive?, J. Geophys. Res., 115, D16117, https://doi.org/10.1029/2010JD013817, 2010.

Zelinka, M. D., Zhou, C., and Klein, S. A.: Insights from a refined decomposition of cloud feedbacks, Geophys. Res. Lett., 43, 9259-9269, https://doi.org/10.1002/2016GL069917, 2016.

Figures

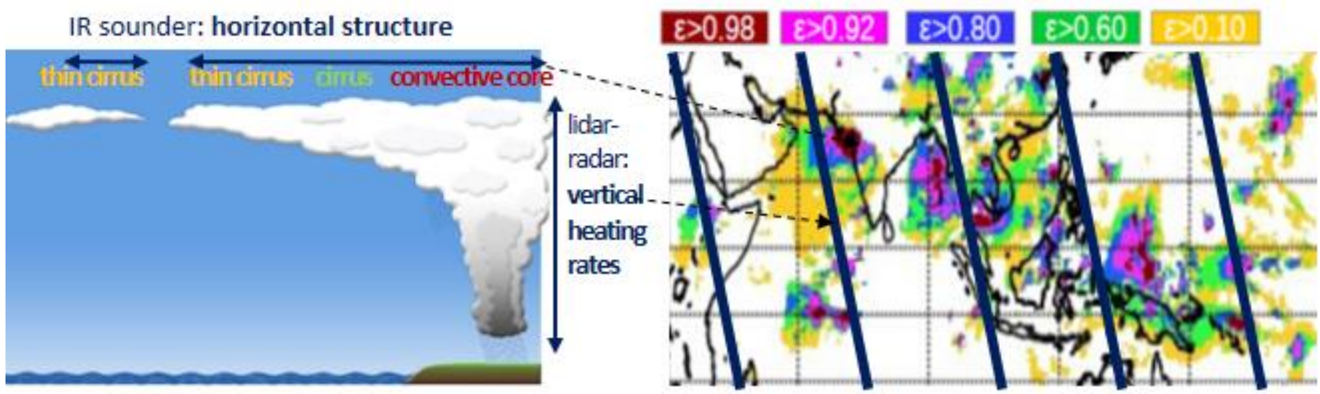

Figure 1: Illustration of three dimensional Cloud System Concept, using spaceborne IR Sounder data (AIRS), providing the horizontal component, and lidar-radar data (CALIPSO-CloudSat), providing the vertical component, both part of NASA's A-Train satellite constellation (left): Based on two independent variables retrieved by AIRS, UT cloud systems are reconstructed from adjacent elements of similar cloud height (p_{cld}), the horizontal emissivity structure allows to directly link the properties of convective cores ($\varepsilon_{cld} > 0.98$) and cirrus anvils (right). Clear sky and low-level cloud fields are also identified (Fig. 4a of Protopapadaki et al. 2017). A horizontally complete picture of the vertical radiative heating rates will be obtained by laterally expanding them, as they are only available along narrow lidar-radar tracks (dark blue). Therefore we have developed optimized 'non-linear regression models', using deep neural network learning techniques, described in section 2.5 and evaluated in section 3, to relate the most suitable cloud and atmospheric properties from IR sounder and meteorological reanalyses to these heating rates.

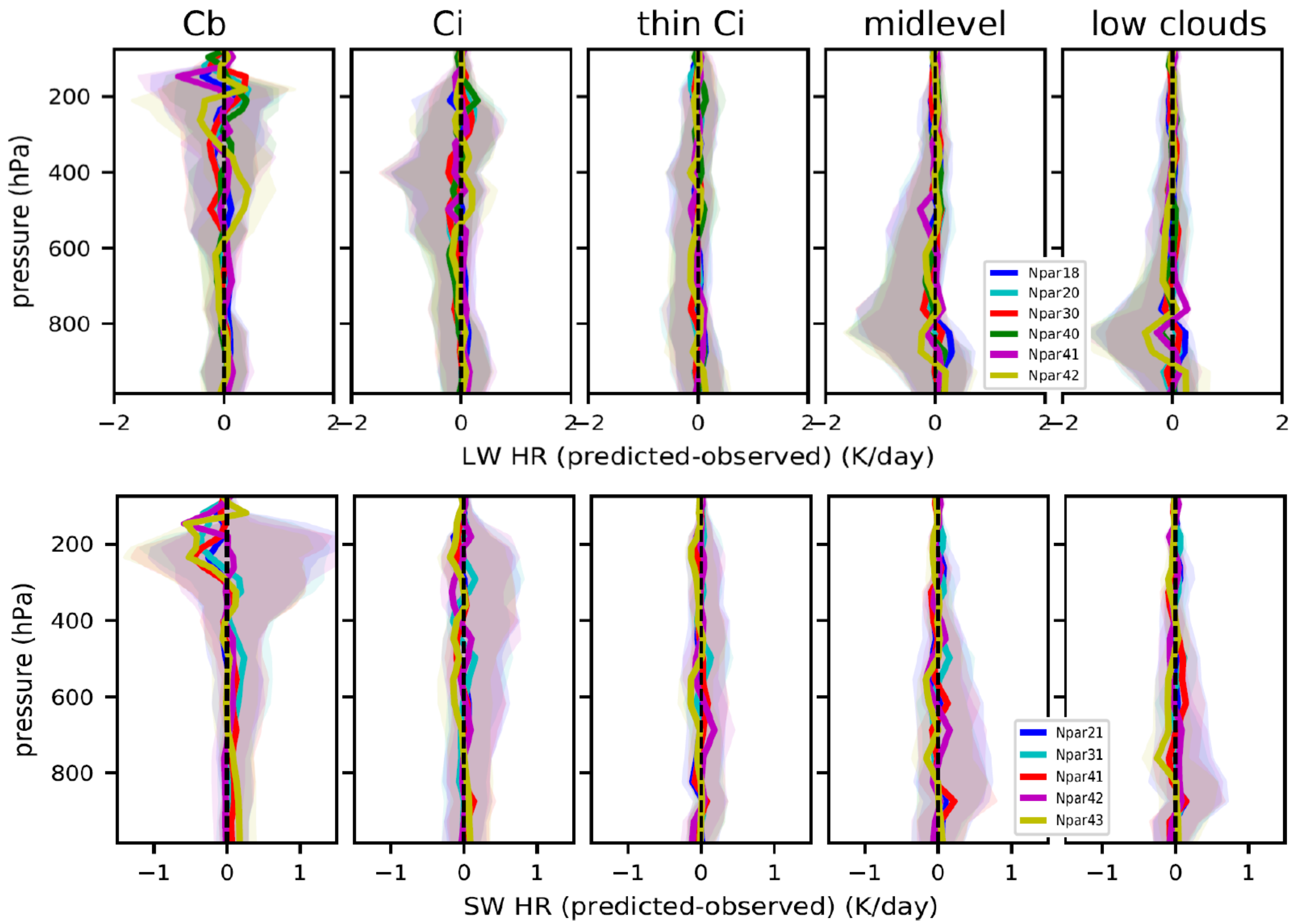

Figure 2: Sensitivity results concerning surface, atmospheric and cloud input parameters for the prediction of cloud LW radiative heating rates (above) and SW radiative heating rates (below): difference between predicted and observed vertical profiles of the validation dataset, separately for Cb, Cirrus, thin Cirrus, mid- and low-level clouds, as identified by AIRS-CIRS, over tropical ocean. 30% and 70% quantiles of the distributions are also shown. Compared are results of the experiments 1-6 (above) and 2-6 (below), using the input parameters listed in Table 1.

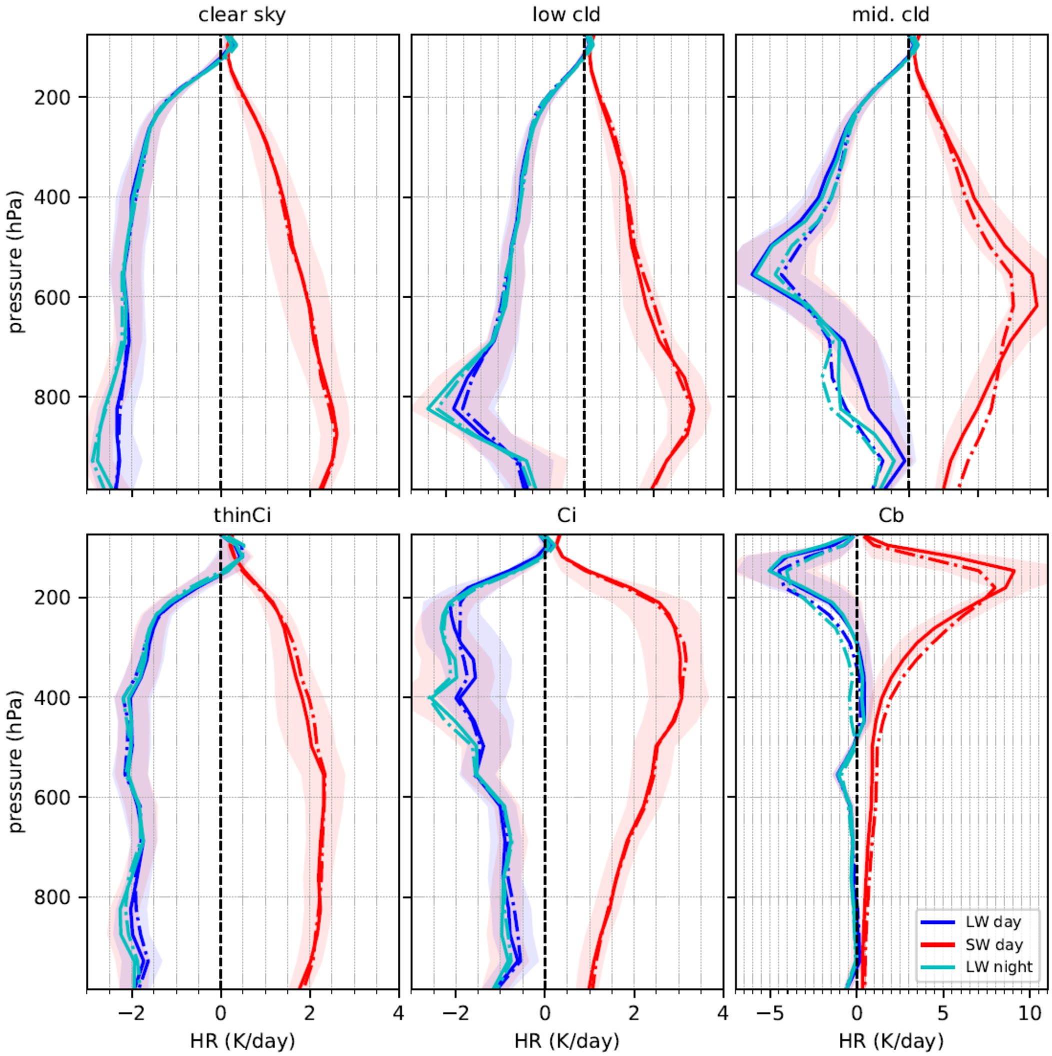

Figure 3: Predicted LW heating rates and SW heating rates (full line), separately for clear sky, low- and mid-level clouds, thin Cirrus, Ci and Cb, as identified by AIRS-CIRS, averaged over the AIRS swaths within 30N – 30S, in January 2008. 30% and 70% quantiles of the distributions indicate their variability. The model has been trained individually over Cb, Ci / thin Ci and mid- / low-level clouds, separately over ocean and land. Broken lines correspond to the average of FLXHR heating rates averaged along the CALIPSO-CloudSat nadir tracks. Night corresponds to 1:30 AM and day to 1:30 PM local time.

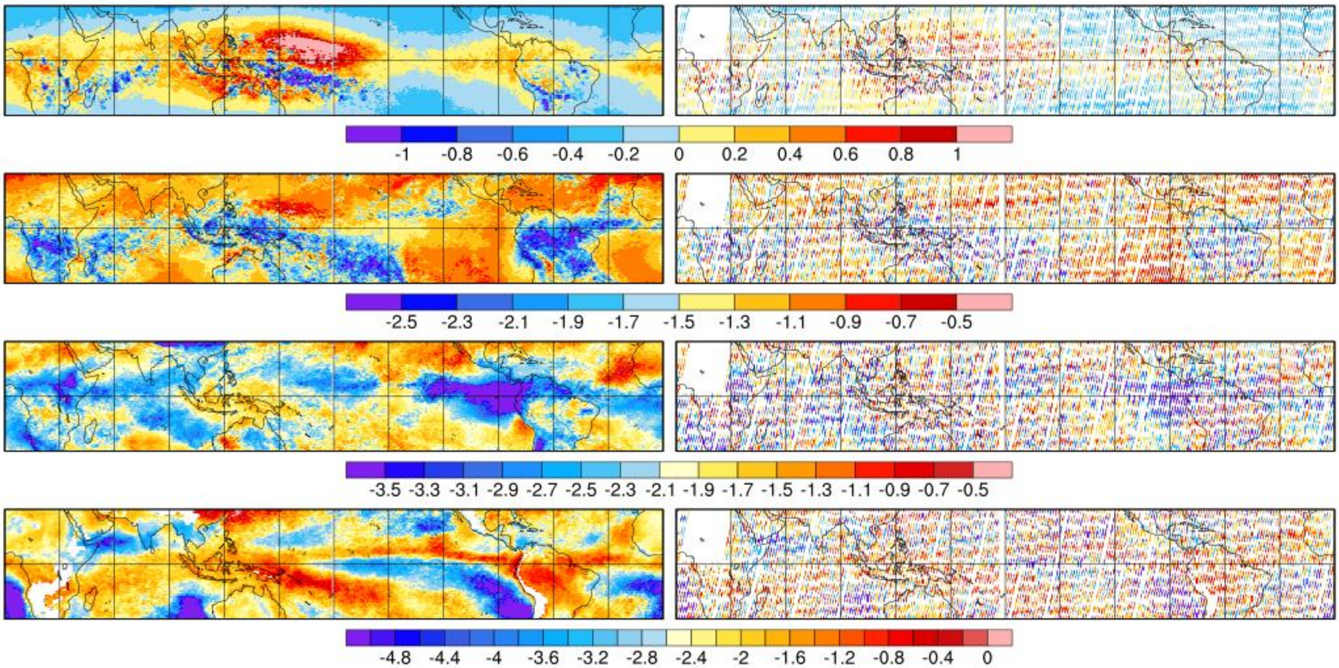

Figure 4: Geographical maps of LW heating rates (K/day) in 4 layers: 106-131 hPa, 200-223 hPa, 525 – 585 hPa and 850 – 900 hPa (from top to bottom) averaged over January 2008 at 1:30AM. Left: predicted over the AIRS swath, using the combination of the eight models developed for Cb, Ci / thin Ci, mid- / low-level clouds and clear sky, separately over ocean and over land. Right: from NASA FLXHR data along the CALIPSO-CloudSat nadir tracks.

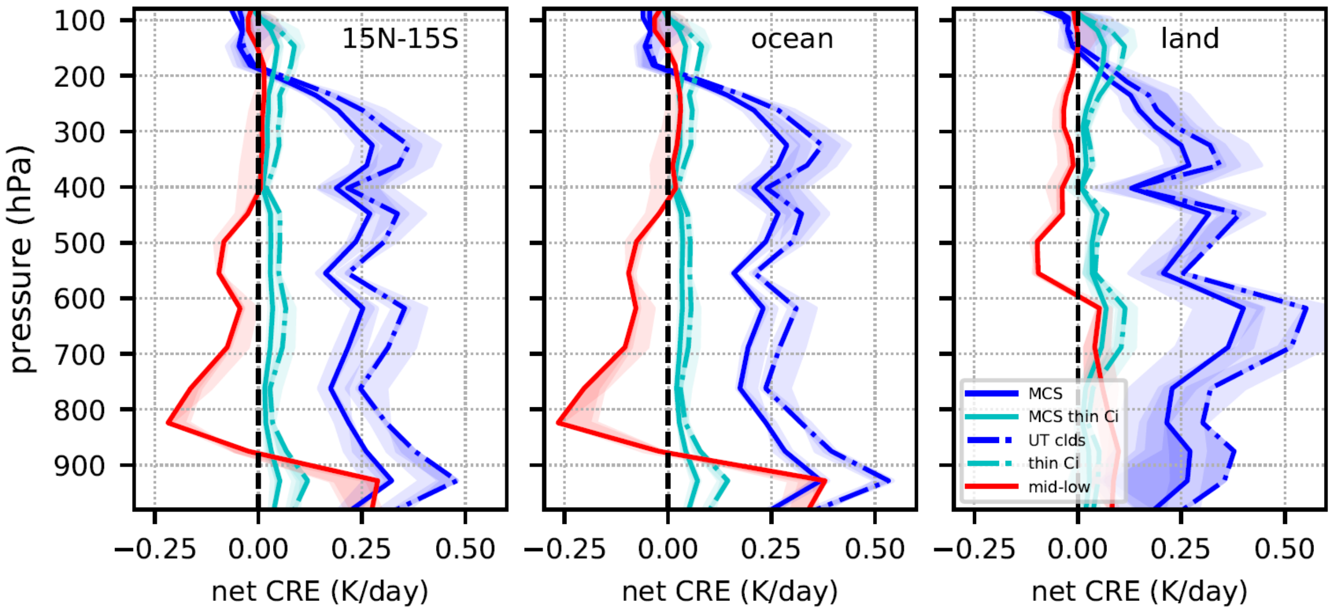

Figure 5: Tropical mean net radiative heating effect within the troposphere of low- and mid-level clouds (red) and UT clouds (blue, broken line), for the latter the effect of MCSs (blue), thin cirrus surrounding MCSs (cyan, full line) and all thin cirrus (cyan, broken line) is shown separately. Left: all, middle: ocean, right: land. Cloud observations at 1:30PM local time, with SW radiation normalized to 24 hours, similar to Li et al. (2013). Statistics of 15 years (2004 – 2018), averaged over 15N to 15S. The sum of UT cloud and mid- / low-level cloud contributions corresponds to the total cloud heating effect, defined as the difference between total and clear sky heating.

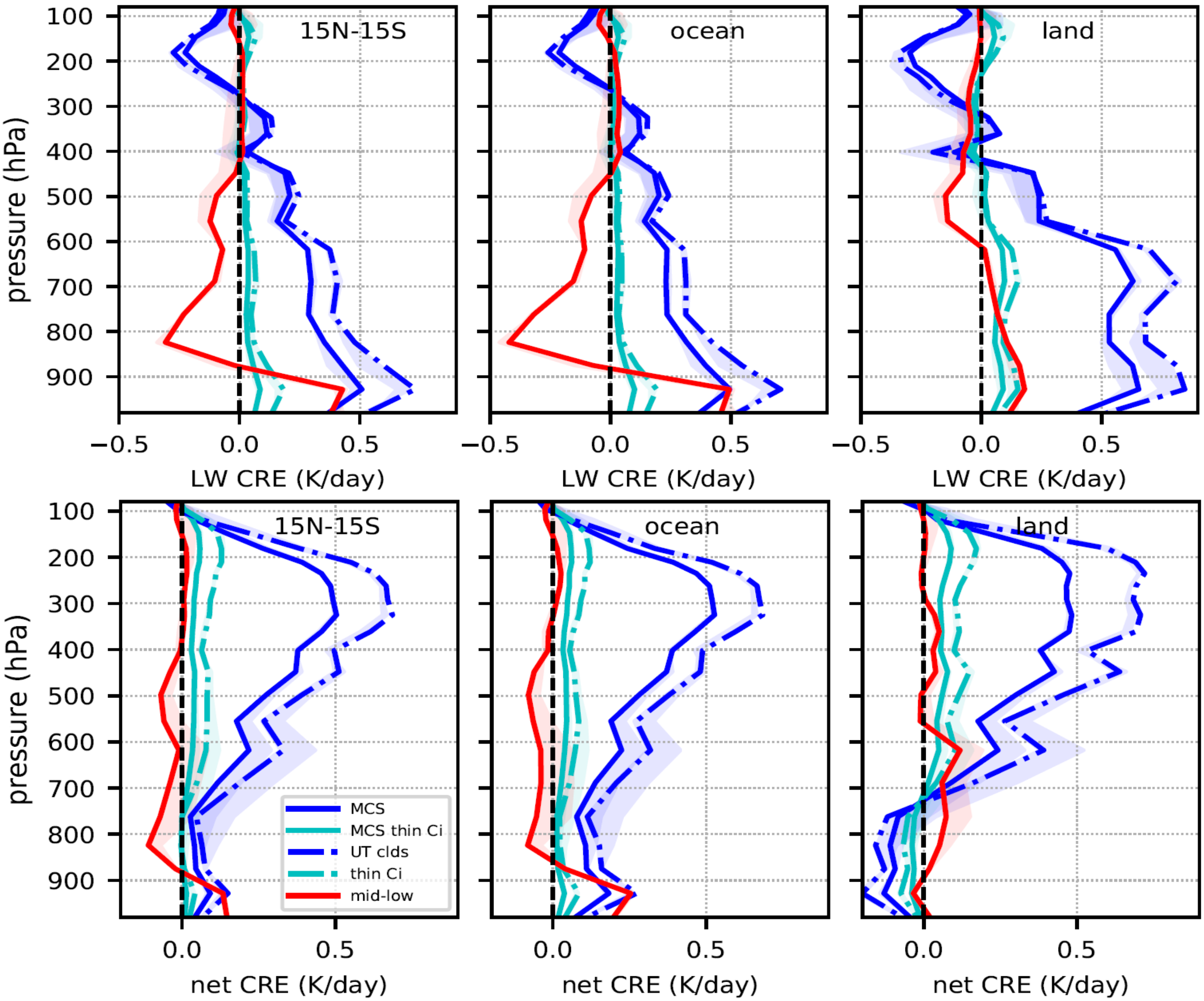

875 **Figure 6: Tropical mean net radiative heating effect within the troposphere of low- and mid-level clouds (red) and UT clouds (blue, broken line), for the latter the effect of MCSs (blue), thin cirrus surrounding MCSs (cyan, full line) and all thin cirrus (cyan, broken line) is shown separately. Left: all, middle: ocean, right: land. Above: at 1:30AM local time, below: at 1:30PM local time. Statistics of 15 years (2004 – 2018), averaged over 15N to 15S.**

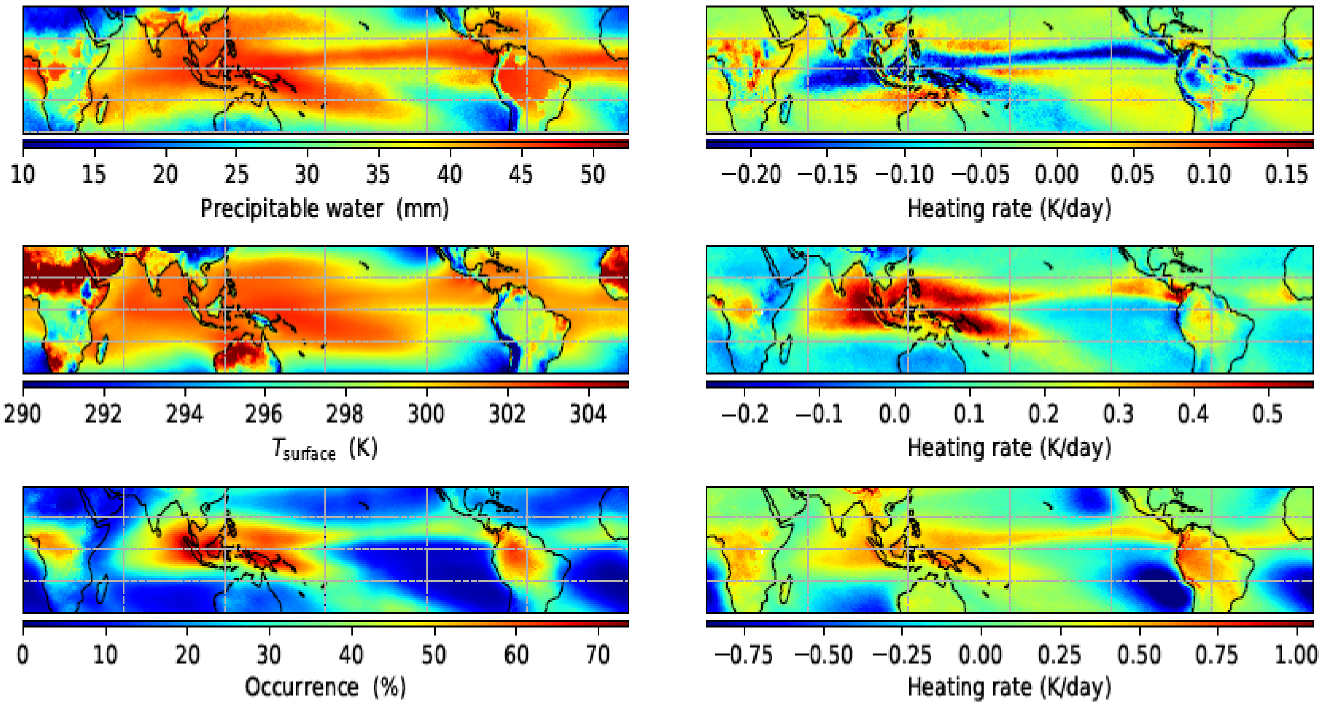

880 **Figure 7: Geographical maps of total precipitable water and surface temperature from ERA-Interim and frequency of occurrence of UT clouds from CIRS-AIRS (left) and of 24-hr net cloud radiative heating effect in three atmospheric layers, integrated over 106 to 200 hPa, over 200 to 585 hPa and 585 to 900 hPa (right). Statistics of 16 years (2003-2018).**

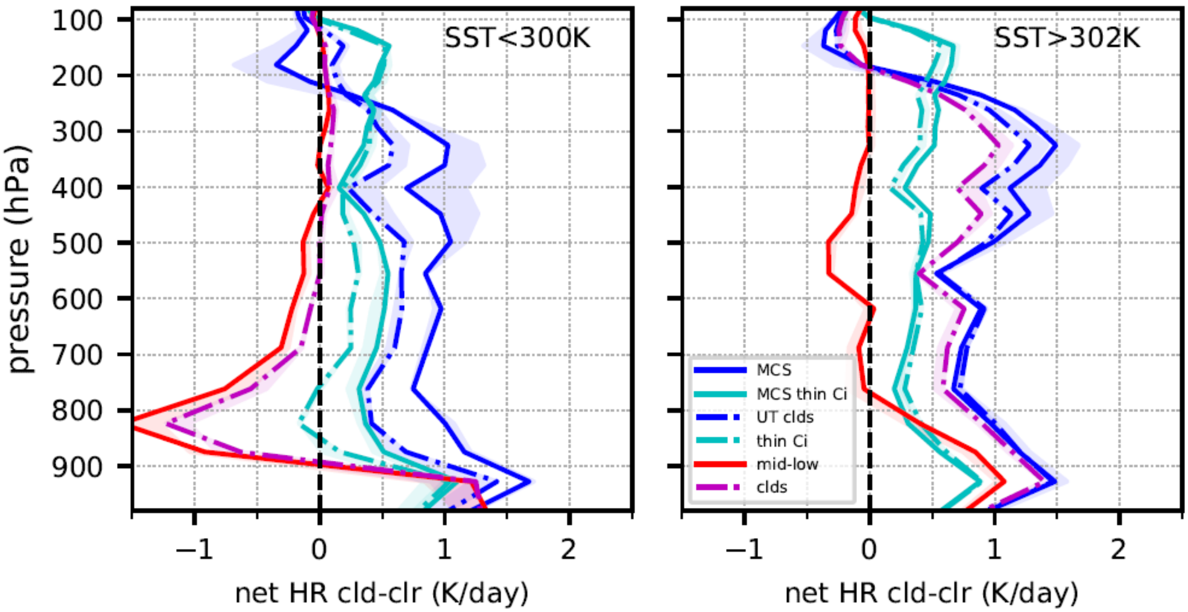

Figure 8: Tropical 24-hour mean cloud net radiative heating effect (magenta) within the troposphere above ocean, as well as the separate effects of low- and mid-level clouds (red), all UT clouds (blue dash-dotted), thin cirrus (cyan dash dotted), MCS (blue full line) and thin cirrus associated with MCS (cyan full line), averaged over 15N to 15S, when the specific cloud types are present. Left: regions with SST < 300 K, right: regions with SST > 302 K. These thresholds correspond to the 30% coolest and warmest tropical oceanic regions.

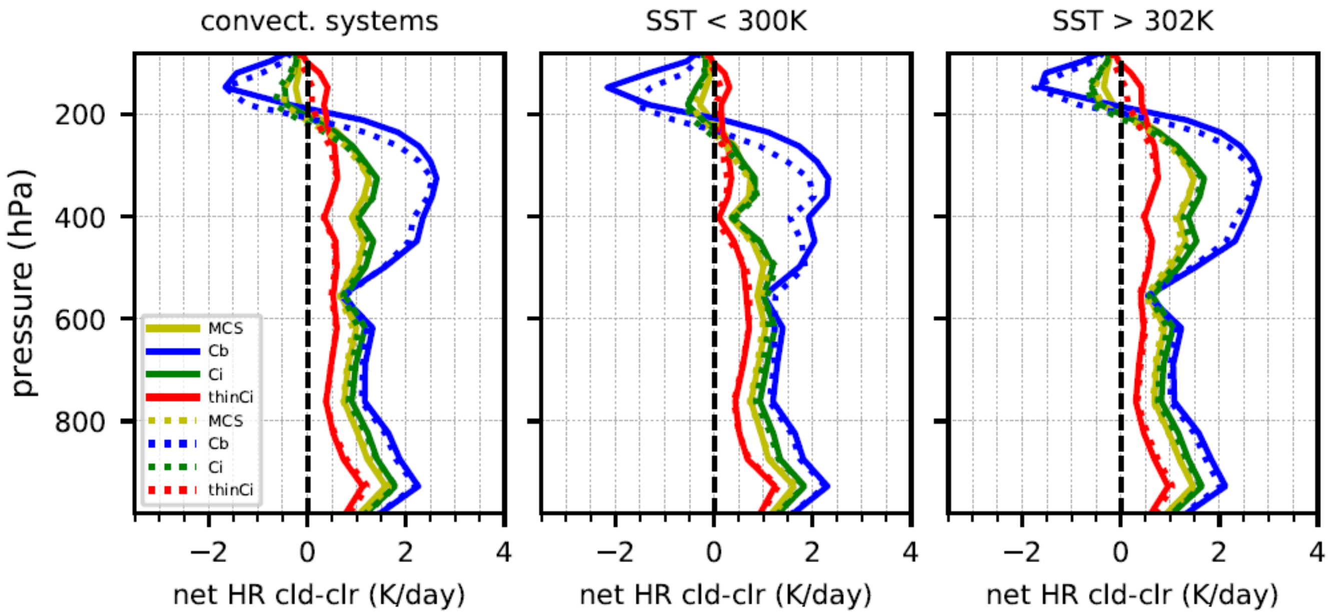

Figure 9: Mean 24-hr net radiative heating effect of tropical maritime MCSs, when present, and their convective cores (Cb), cirrus anvil (Ci) and surrounding thin cirrus (thinCi), separately for all MCS (full line) and for those with single convective cores (dotted lines). Further are distinguished MCSs over the 30% coolest areas (SST < 300K) and over the 30% warmest areas (SST > 302K). Statistics of 15 years (2004-2018), averaged over 15N to 15S.

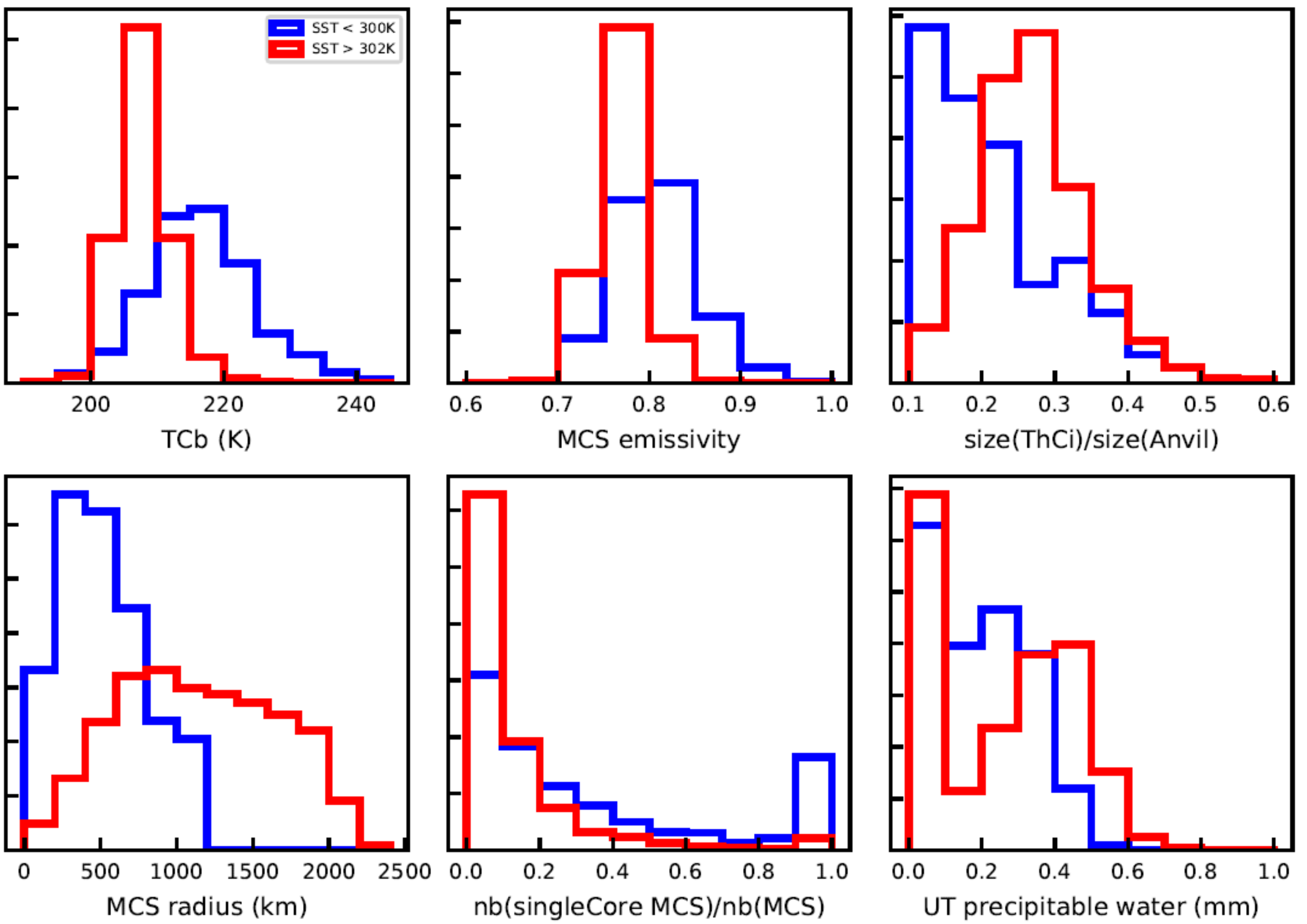

Figure 10: Normalized distributions of maritime MCS properties: near cloud top temperature of convective cores, emissivity of convective cores and cirrus anvil, relative size of thin cirrus surrounding the anvil, radius of convective core and cirrus anvil, fraction of MCSs with single convective core, upper tropospheric precipitable water, separately for systems overlying cool and warm regions.

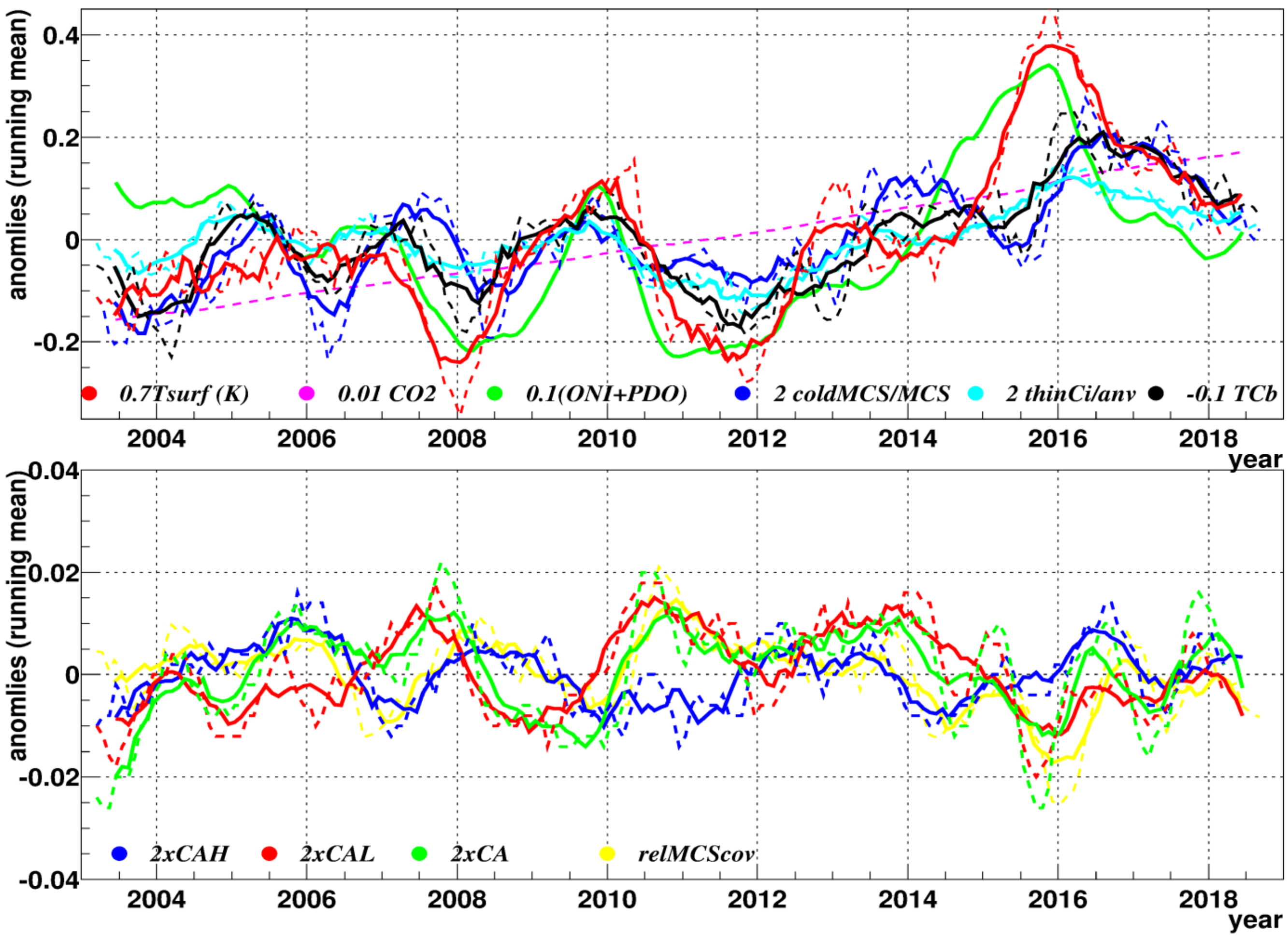

Figure 11: Top: Time series of 12-month running means (bold lines) and 6-month running means of deseasonalized anomalies of tropical surface temperature (ERA-Interim), ENSO index (ONI) and Inter-decadal Pacific Oscillation (PDO) index, as well as coverage of cold MCSs over all MCSs (multiplied by 2), area of thin cirrus over area of total cirrus anvil (multiplied by 2), convective core temperature (in K, multiplied by -0.1) and increase of CO_2 concentration (in ppm, multiplied by 0.01). Bottom: Time series of 12-month running means of deseasonalized anomalies of cloud cover (CA), UT cloud cover (CAH) and low-level cloud cover (CAL), multiplied by 2, and of relative MCS coverage.

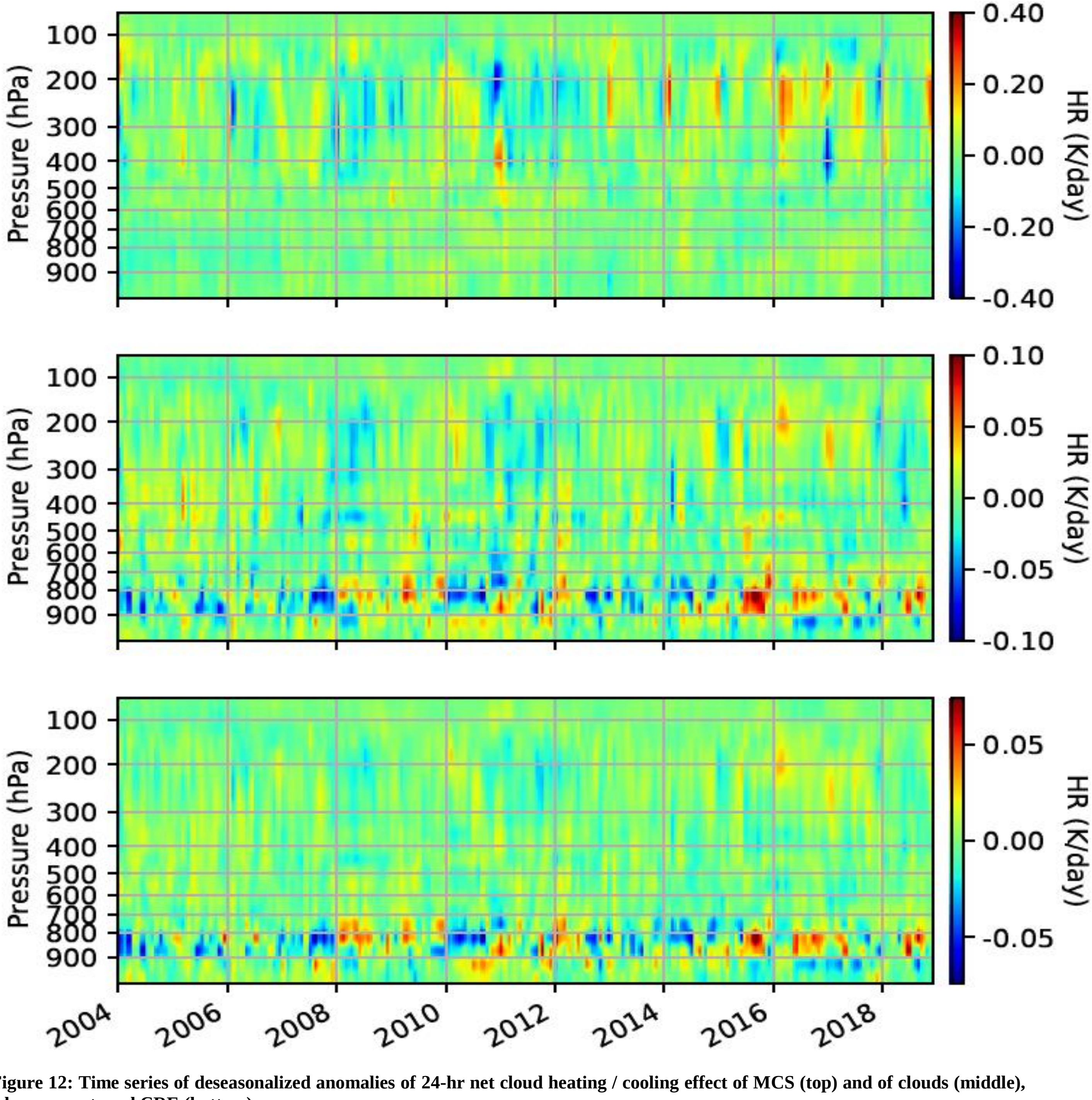

910 **Figure 12: Time series of deseasonalized anomalies of 24-hr net cloud heating / cooling effect of MCS (top) and of clouds (middle), when present, and CRE (bottom).**

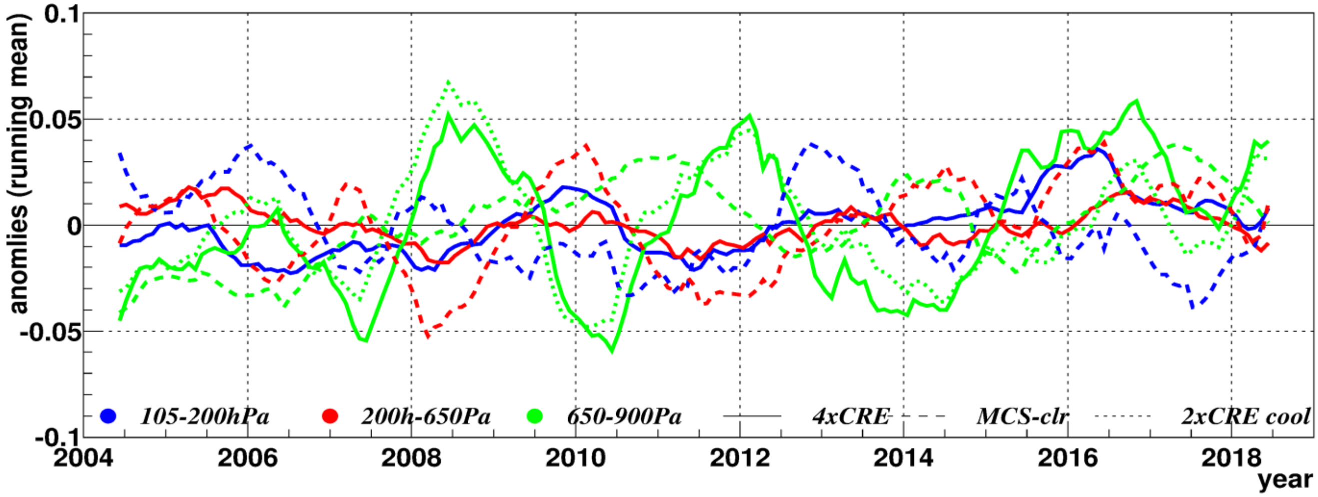

Figure 13: Time series Time series of 12-month running means of deseasonalized anomalies of 24-hr net cloud heating / cooling effect of CRE (full lines) and MCS (broken lines), over three vertical layers, and of CRE in boundary layer (650-900 hPa) over cool regions (green dotted line).

915

Supplement of

3D Radiative Heating of Tropical Upper Tropospheric Cloud Systems derived from Synergistic A-Train Observations and Machine Learning

Claudia J. Stubenrauch[1], Giacomo Caria[1], Sofia E. Protopapadaki[2], Friederike Hemmer[1]

[1]Laboratoire de Météorologie Dynamique / Institut Pierre-Simon Laplace, (LMD/IPSL), Sorbonne Université, Ecole Polytechnique, CNRS, Paris, France
[2]COOPETIC, Paris, France

Correspondence to: Claudia J. Stubenrauch (stubenrauch@lmd.polytechnique.fr)

Figures S1 and S2 present the MAE as a function of number of iterations (epochs), for cloudy scenes and for clear sky scenes, respectively. The similarity in MAE between the validation and testing data means that there is no underfitting (the variables are not sufficient to predict the target) nor overfitting (the model is too detailed, with too many variables or the data base is not sufficiently large). The number of epochs to converge towards a minimum loss is relatively small: less than 60 for cloudy scenes (Figure S1) and less than 45 for clear sky scenes (Figure S2). Essentially, the MAE decreases considerably only within the first 10 (5) epochs for cloudy (clear sky) scenes. The relatively small number of epochs necessary for convergence may be explained by the large statistics we use for the training and the number of relevant variables for the prediction. The final choice of parameters corresponds to Npar40 / Npar41 in Figure S1, as the MAE is smallest and comparable with the ones of Npar41 / Npar42 and Npar42 / Npar43. For clear sky scenes, Figure S3 compares the evolution of MAE for models developed over ocean over land and over both. Figure S2 shows that predictions over ocean will be better than over land which can be explained by a better homogeneity. Figure S2 also shows that by using the atmospheric profiles with a better vertical resolution (20 layers instead of 10) does not improve the results.

For LW / SW: Npar18 / Npar19 = basic, Npar20 / Npar21 =+CR, Npar30 / Npar31 =+RH10
Npar40 / Npar41 =+T10, Npar41 / Npar42 =+w500, Npar42 / Npar43 =+AOD

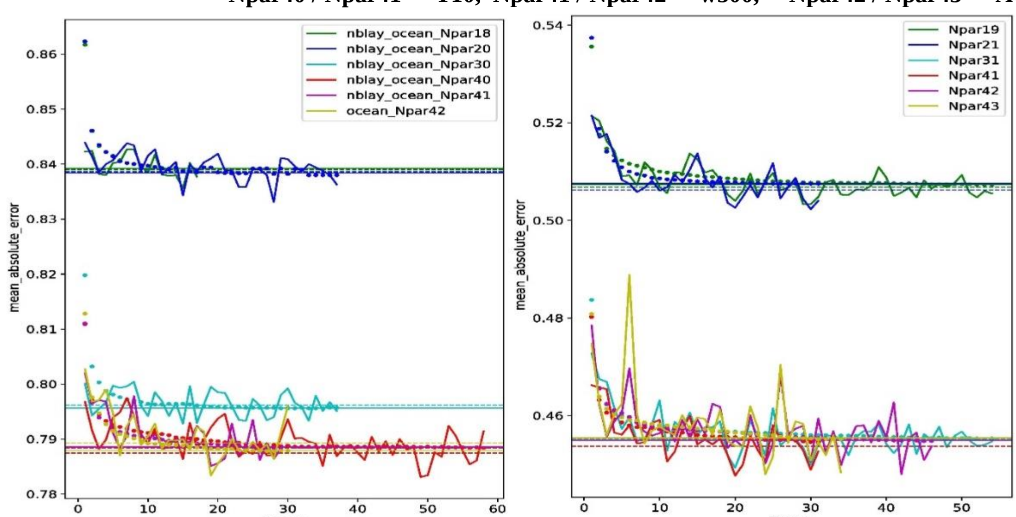

Figure S1: Sensitivity results concerning surface, atmospheric and cloud input parameters for the prediction of LW (left) and SW (right) radiative heating rates of clouds over ocean: Mean absolute error (in K/day) of training (dots) and validation (lines) for the experiments 1-6 for LW and 2 – 6 for SW, using the parameters listed in Table 1.

For LW / SW: **ocean_Npar35 / Npar35 = clear sky basic without cloud properties + clear sky fraction of CR + RH10 + T10, land_Npar38 / Npar36 = as for ocean, + 3 IR surface emissivities / + 1 surface albedo**
Npar39 / Npar37 = for land and ocean together, including land-ocean flag
Npar60 / Npar58 = for land and ocean together, RH20 + T20 instead of +RH10+T10

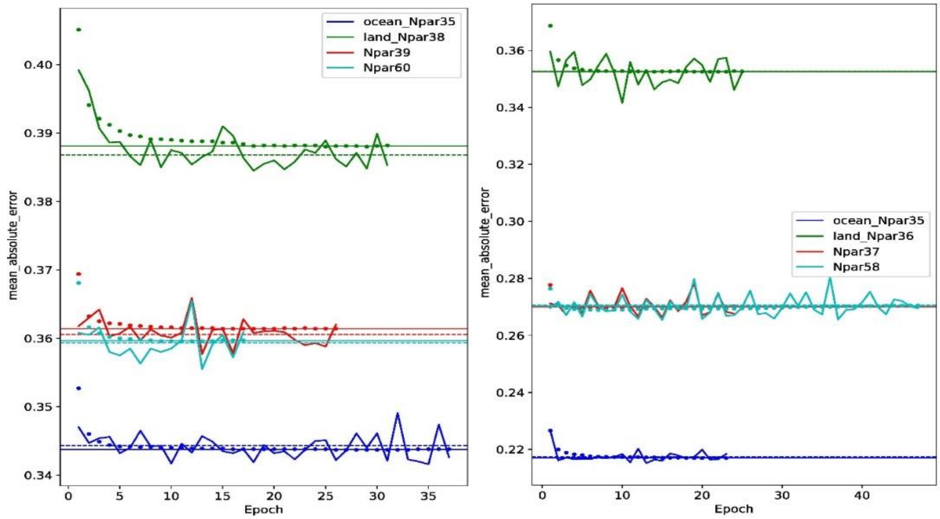

Figure S2: Sensitivity results for the prediction of LW (left) and SW (right) radiative heating rates of clear sky scenes as determined by CIRS: Mean absolute error (in K/day) of training (dots) and validation (lines): for the parameters listed in Table 1, excluding cloud properties and their uncertainties.

Sensitivity to the selection of scenes used for the training

These sensitivity studies are dedicated to the scene types for which we develop the models:

i) all clouds over the whole tropical band (one model)

ii) all clouds separately over ocean and over land (two models)

iii) high-level clouds and mid- / low-level clouds individually, each separately over ocean and over land (four models)

iv) Cb, Ci / thin Ci, mid- / low-level clouds individually, each separately over ocean and over land (six models)

In addition, we develop models for clear sky i) over the whole tropical band (one model) and ii) separately over ocean and over land (two models). In general, a model trained over all scenes together soothes out differences between different cloud types and between ocean and land. Also scenes which are less frequent may have a smaller weight and may be therefore less represented than other scenes. Since we are interested in the study of the effect of UT cloud systems, we choose to use separate models. In particular, the modelling of Cb clouds is improved when exploiting a dedicated training for this cloud type, which represents about 7% of all clouds in the deep tropics (Stubenrauch et al., 2017).

To illustrate the effect of model aptness in dependence of training scenes, we compare in Figure S3 the difference between the predicted radiative HRs and those from CALIPSO-CloudSat over ocean for Cb, cirrus and thin cirrus, in the LW and SW, respectively. Compared are models which were trained i) for all clouds over ocean and land together, ii) for all clouds over ocean, iii) for high-level clouds over ocean and iv) for Cb and for Ci / thin Ci over ocean. All results are quite similar, with the differences between mean predicted and 'observed' radiative HRs undulating well around 0 K/day. However, we observe an overestimation of the LW cooling above Cb clouds by nearly 1 K/day when all clouds together are used to develop one single model. The results improve for cirrus and thin cirrus when a dedicated model is developed for these cloud types. For the SW HRs it is not possible to determine the best performance among these four models. The SW heating in the upper part of Cb clouds is more difficult to predict, as for all four models the mean difference undulates around 0 K/day within ± 0.8 K/day between 100 and 200 hPa. Considering the radiative HR profiles shown in Figure S4 of the supplement, we find that the largest uncertainties for Cb clouds are around the maxima of LW cooling and SW heating. Furthermore, we observe that all models give very similar results, so that in the following we will mainly use the most specific scene models, leading to the application of eight models to reconstruct the radiative heating rate fields over the tropics.

We have also estimated the uncertainty related to the choice of scenes for the training after having applied these different ANN models to one month of AIRS data, over the whole tropical band (30N – 30S). Figure S5 presents for three atmospheric layers the difference between predicted LW HRs obtained from four models (clouds over ocean, clouds over land, clear sky over ocean, clear sky over land) and from two models (clouds and clear sky) and between predicted LW HRs obtained from all final eight models and from the four scene-dependent models. These differences, which give an indication of the uncertainty, lie generally within 0.25 K/day, with only a few regions of 0.45 K/day, keeping in mind that the most detailed scene distinction will give the better results.

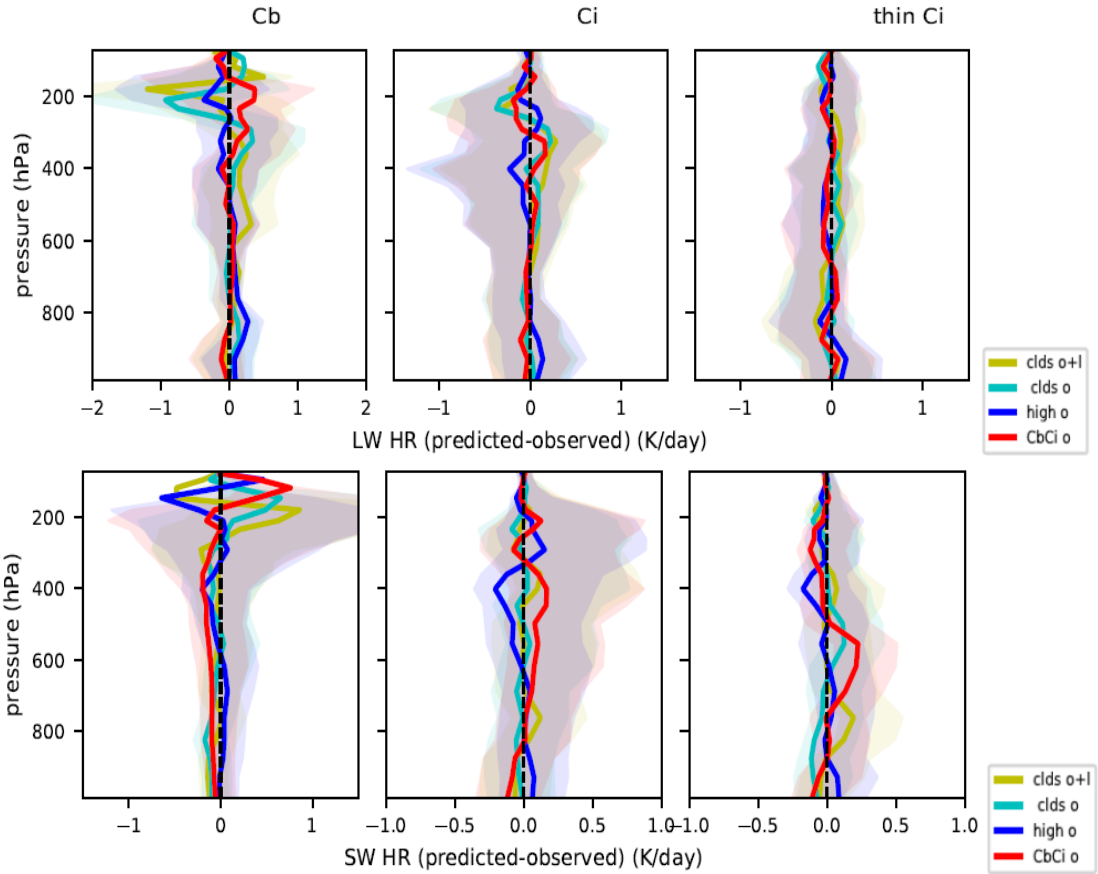

Figure S3: Sensitivity results concerning training over different scenes (high clouds over ocean, all clouds over ocean and all clouds over ocean and land) for the prediction of high-level cloud LW radiative heating rates (above) and SW radiative heating rates (below): difference between predicted and observed vertical profiles, separately for Cb, Cirrus and thin Cirrus, as identified by AIRS-CIRS, over tropical ocean. 30% and 70% quantiles of the distributions are also shown.

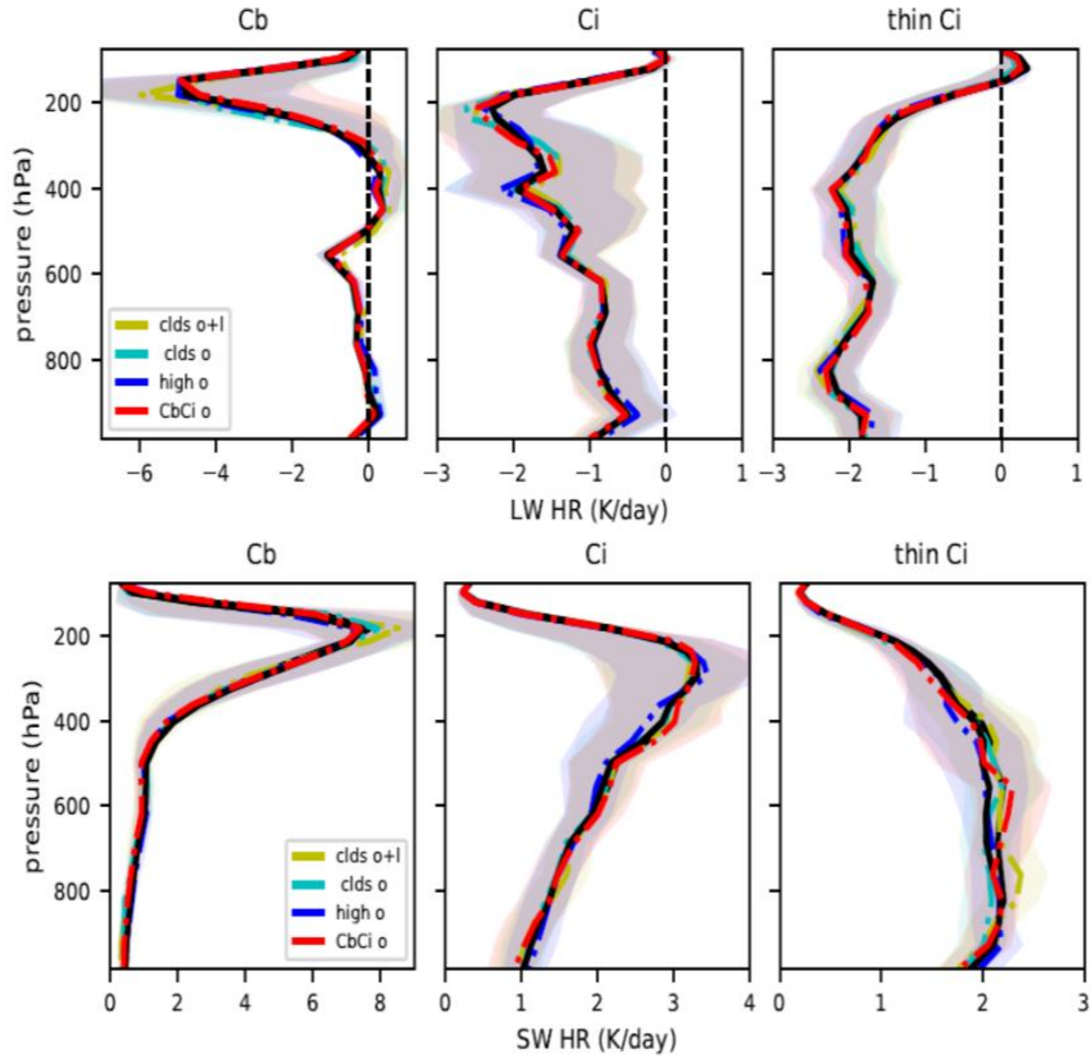

Figure S4: Sensitivity results concerning training over different scenes (high clouds over ocean, all clouds over ocean and all clouds over ocean and land) for the prediction of high-level cloud LW radiative heating rates (above) and SW radiative heating rates (below): predicted vertical profiles compared to those from CALIPSO-CloudSat (black lines), separately for Cb, Cirrus and thin Cirrus, as identified by AIRS-CIRS, over tropical ocean. 30% and 70% quantiles of the distributions are also shown.

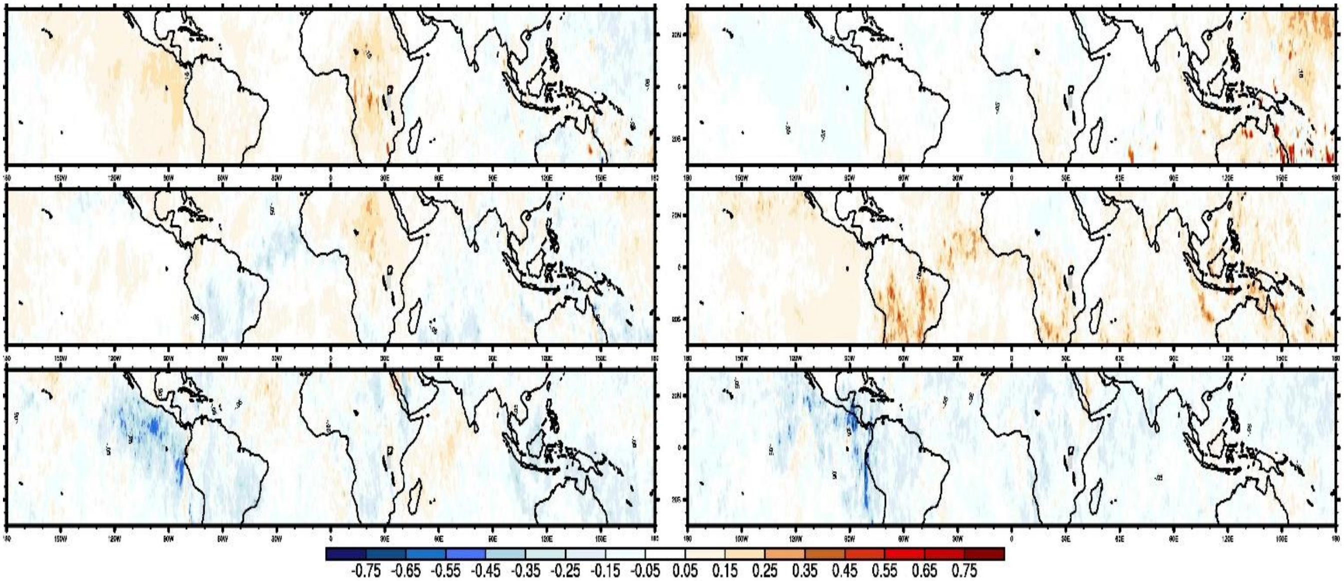

Figure S5: LW heating rate differences in 3 layers (106-131 hPa, 200-223 hPa, 525-585 hPa) between combination of (left) 4 models (clouds over ocean, clouds over land, clear sky over ocean, clear sky over land) and of 2 models (clouds and clear sky) and (right) 8 models and 4 models (clouds over ocean, clouds over land, clear sky over ocean, clear sky over land).

Since the AIRS clear sky identification may also include subvisible cirrus as well as partly cloudy scenes within the AIRS footprint, we estimated how much this affects the radiative HRs by comparing the FLXHR-lidar HRs for AIRS clear sky and for CALIPSO-CloudSat clear sky identification (no GEOPROF-lidar cloud layer within the footprint). Definitely, Figure S6 shows a slight positive bias in the clear sky LW heating near 100 hPa of about 0.1 to 0.2 K/day due to subvisible cirrus, in particular during night, when the CALIPSO lidar better detects subvisible cirrus. The SW clear sky heating positive bias of the same order of magnitude between 200 and 800 hPa and the cold LW clear sky heating negative bias around 900 hPa are most probably linked to contamination by partial cloudiness. As our present HR data are stored at a spatial resolution of 0.5°, we have identified another bias, which is due to the identification of clear sky at a spatial resolution of 0.5°. Clear sky HRs are sampled only over grid boxes with all AIRS footprints identified as clear sky. The broken lines in Figure S6 present the difference between the average HRs, deduced by machine learning and averaged over 0.5° for cases with clear sky fraction equal to 1, and the average FLXHR-lidar HRs along the nadir tracks for the cases with CALIPSO-CloudSat clear sky identification. This gives an estimation of the biases due to sampling at coarse spatial resolution and effects on the machine learning.

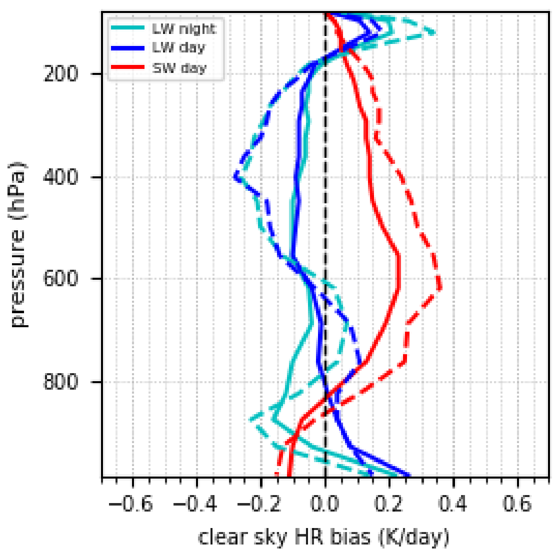

Figure S6: Bias in LW and SW heating rates due to uncertainties in CIRS clear sky identification (full line), given as mean difference of FLXHR radiative heating rates of clear sky identified as no CloudSat-lidar GEOPROF cloud layers and of 'clear sky – partly cloudy' identified by AIRS using the CIRS 'a posteriori' cloud detection, and in addition the effect of sampling for clear sky fraction 1 over 0.5 ° (broken line), separately at nighttime (1:30 AM LT) and at daytime (1:30 PM LT). Statistics is over January 2008.

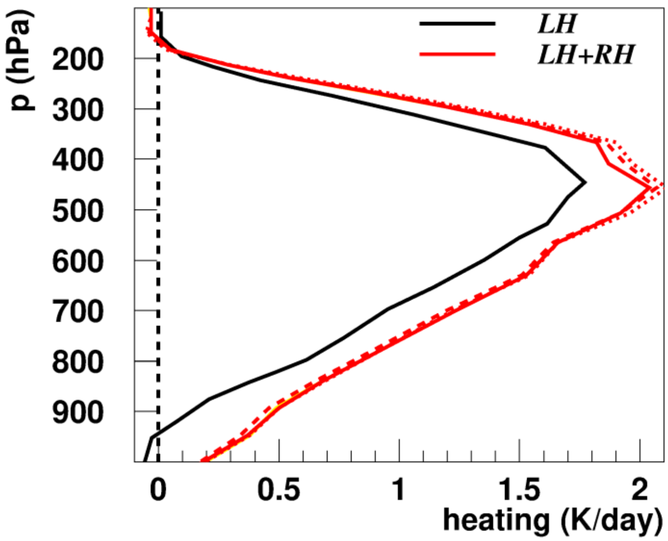

Figure S7: Tropical mean latent heating (black), digitized from Figure 9 of Li et al. (2013), and tropical mean diabatic
1040 **heating (red) as the sum of latent heating and net radiative heating (from Figure 5), including uncertainties due to cloud cover variation (dotted), LW HR variability between night and day (broken) and clear sky identification bias (only visible as slightly larger contribution near the surface and near the troposphere).**

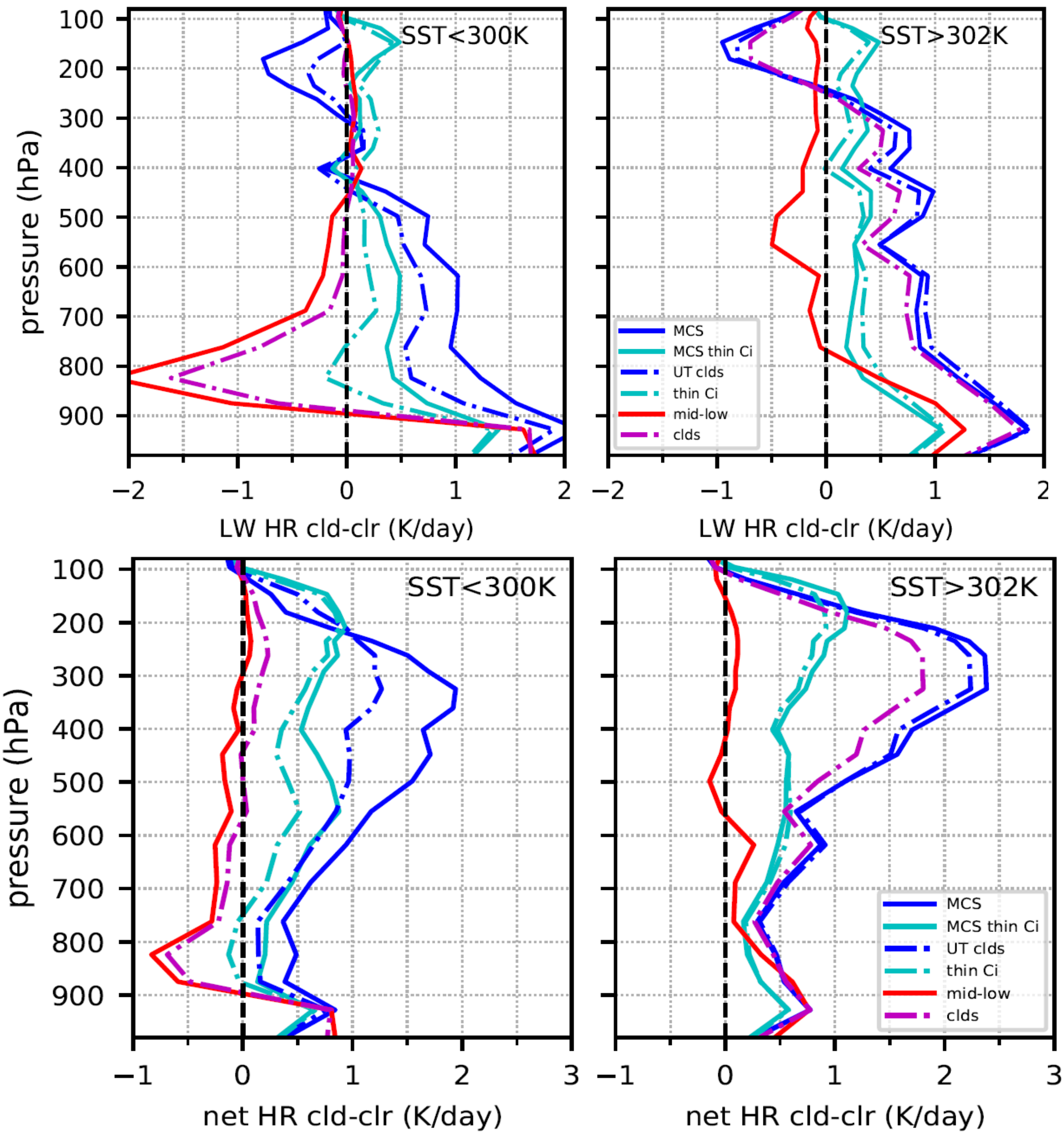

Figure S8: Tropical mean cloud net radiative heating effect (magenta) within the troposphere above ocean at 1:30 AM LT (top) and at 1:30 PM LT (bottom), as well as the separate effects of low- and mid-level clouds (red), all UT clouds (blue dash-dotted), thin cirrus (cyan dash dotted), MCS (blue full line) and thin cirrus associated with MCS (cyan full line), averaged over 15N to 15S, when the specific cloud types are present. Left: regions with SST < 300 K, right: regions with SST > 302 K.

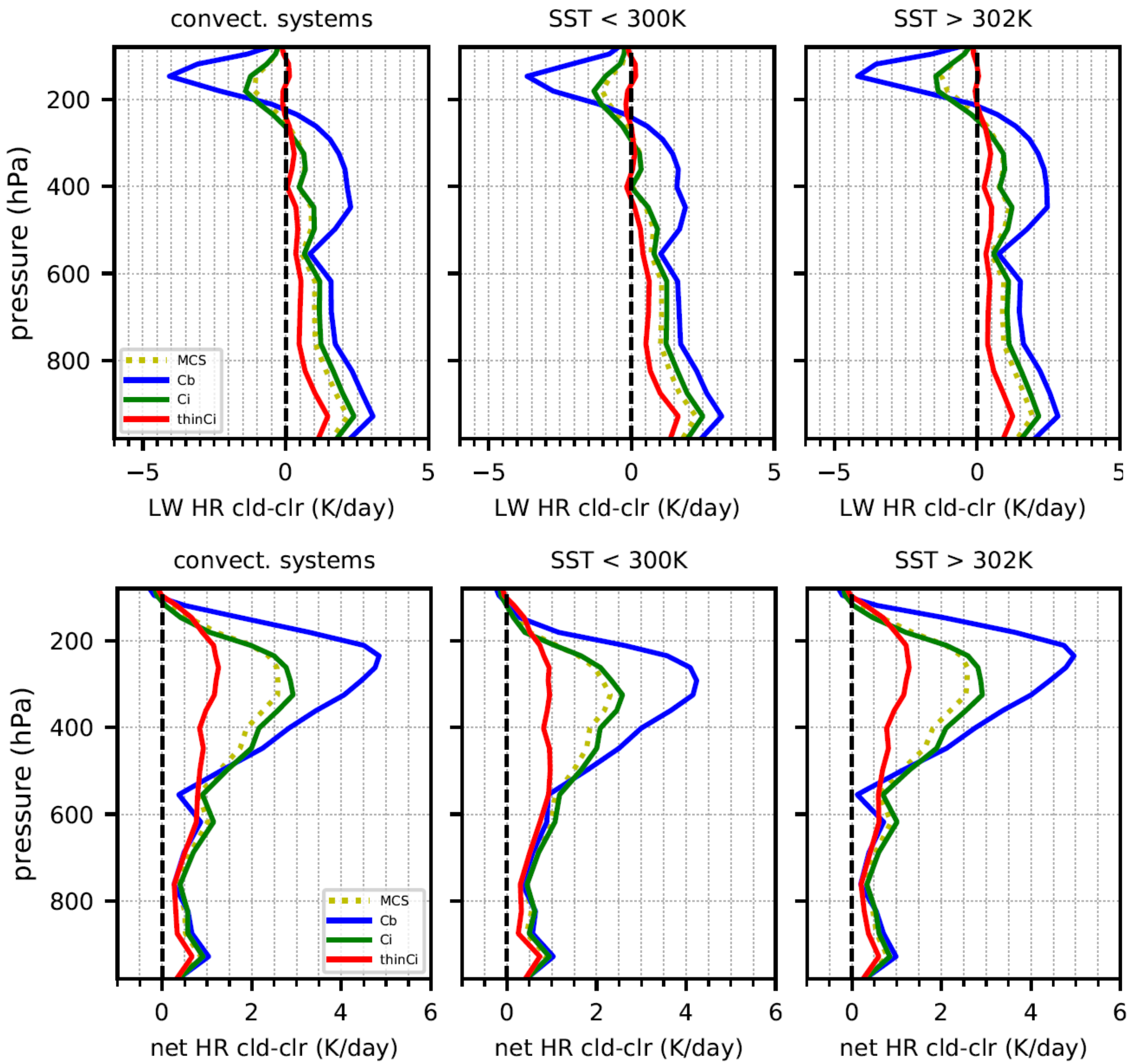

1055

Figure S9: Mean net radiative heating effect of maritime MCSs, when present, and their convective cores (Cb), cirrus anvil (Ci) and surrounding thin cirrus (thinCi) at 1:30AM LT (top) and at 1:30 PM LT (bottom). Compared to MCSs over cool areas (SST < 300K) and to MCSs over warm areas (SST > 302K). Statistics of 15 years (2004-2018).

1060

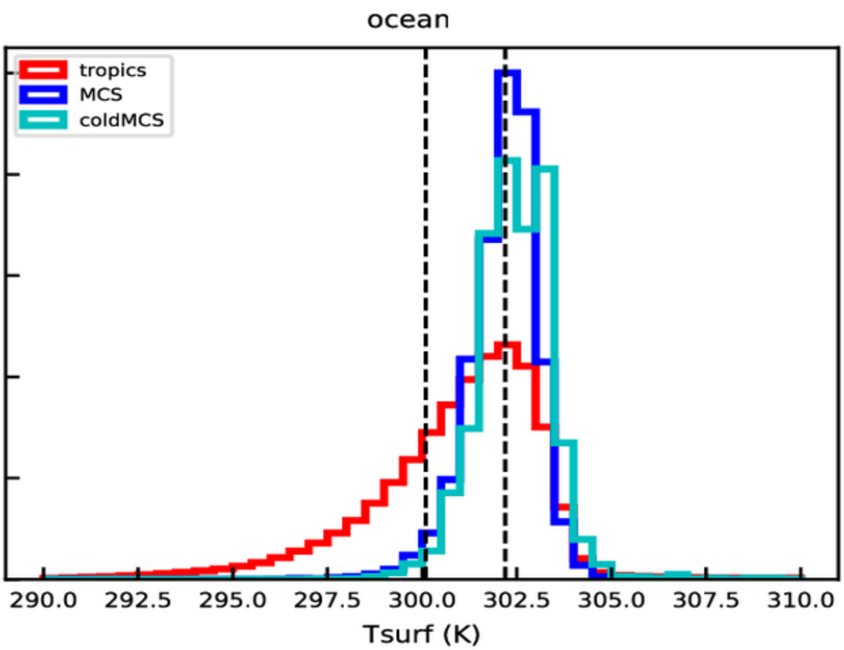

Figure S10: Normalized distributions of surface temperature (ERA-Interim) over tropical ocean (20N-20S) and of surface temperature underneath the opaque part (cloud emissivity > 0.9) of all MCSs and of cold MCS (cloud temperature of opaque part < 210K). The black lines correspond to the threshold temperatures for the 30% coolest and 30% warmest surface temperatures, 300K and 302K, respectively. 15 years statistics averaged over 1:30 AM and 1:30 PM LT.

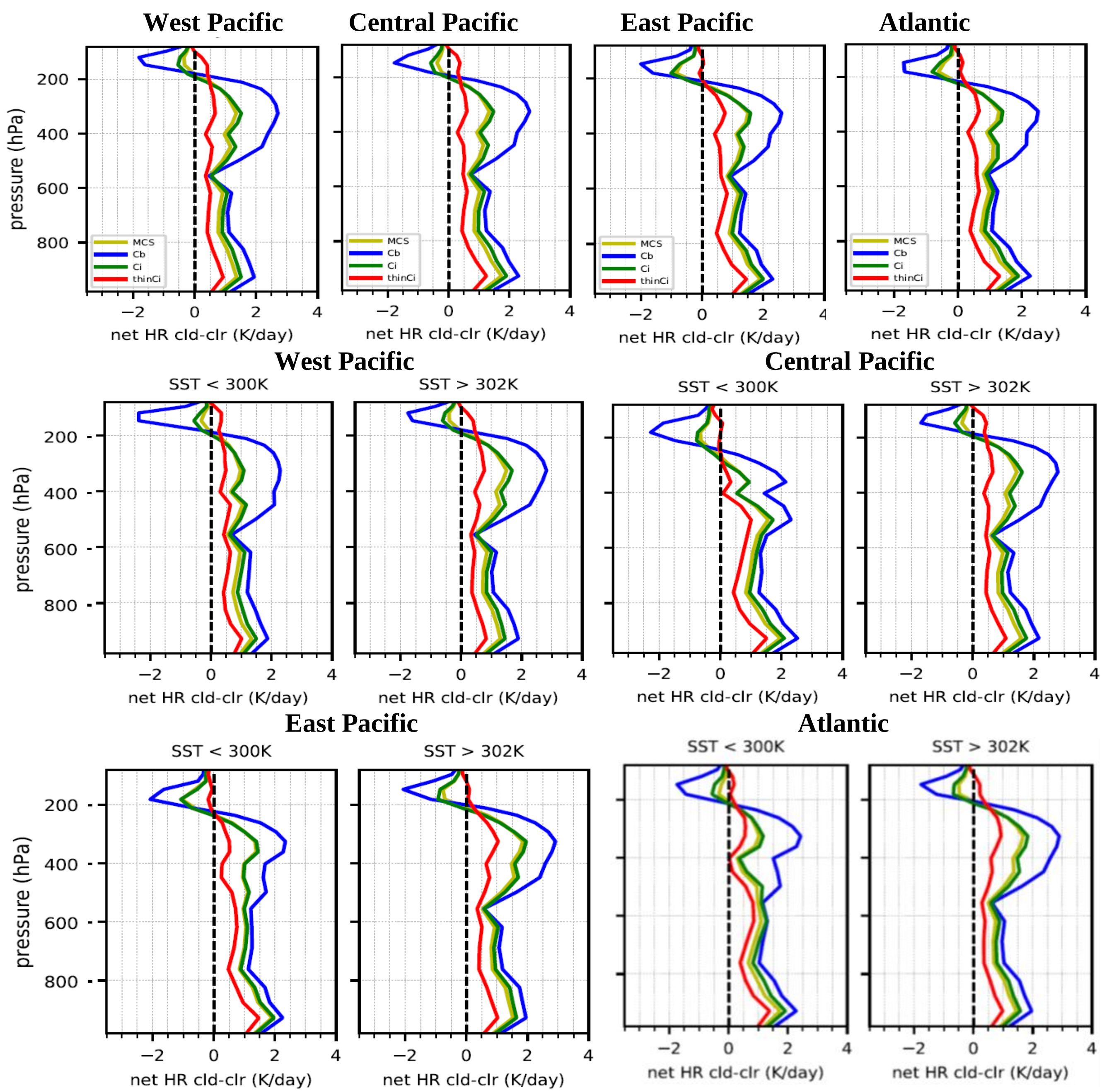

Figure S11: Mean 24-hr net radiative heating effect of maritime MCSs, when present, and their convective cores (Cb), cirrus anvil (Ci) and surrounding thin cirrus (thinCi). First panel from left to right: over four specific regions (West Pacific: 12N-12S and 130E-170E; Central Pacific: 10N-10S and 150W-180W; Eastern Pacific: 10N-10S and 100W-130W; Atlantic: 10N-10S and 5W-35W). Second and third panel: each of these regions separately over cool areas (SST < 300K) and over warm areas (SST > 302K). Statistics of 15 years.